Development and high-power operation of the cw 250 kW fundamental power couplers on 166.6 MHz quarter-wave SRF cavities at the High Energy Photon Source

Tongming Huang,[1,2] Pei Zhang,[1,2,*] Qiang Ma,[1,2] Xinying Zhang,[1,2] Haiying Lin,[1] Qunyao Wang,[1,2] Dongbing Li,[1] Facheng Zhao,[1] and Fanbo Meng[1]

[1]*Accelerator Division, Institute of High Energy Physics (IHEP), CAS, Beijing 100049, China*
[2]*School of Nuclear Sciences and Technology, University of Chinese Academy of Sciences, CAS, Beijing 100049, China*

(Received 20 September 2026; accepted 27 October 2026; published 10 November 2026)

The High Energy Photon Source (HEPS), a newly commissioned 6 GeV fourth-generation synchrotron light source, employs five 166.6 MHz quarter-wave $\beta = 1$ superconducting cavities in its storage ring. Each cavity requires a fundamental power coupler capable of delivering 200 kW continuous-wave power—a specification largely exceeding demonstrated limits for existing on-cell couplers in transverse electromagnetic (TEM)-type superconducting cavities. This paper presents the complete development, validation, and operation of these couplers from prototype to series production. The design resolves four competing constraints: high power handling, low cryogenic heat load, mitigation of field-emission damage, and cleanroom assembly compatibility. Overheating at the cavity-coupler interface was identified as the primary degradation mechanism during prototype testing. Consequently, Series-A and Series-B design iterations were developed to eliminate interface overheating and window frosting, respectively. These modifications reduced the maximum interface temperature from 15.4 to 10.8 K and halved the average 4.2 K heat load to 1.5 W under nominal operation. All 10 series couplers were validated via high-power testing, with five currently operating stably in the HEPS storage ring at a 150 mA beam current. This represents the highest beam-operation power level reported to date for on-cell couplers in TEM-type superconducting cavities, expanding the application of nonelliptical superconducting cavities in high-current accelerators.

DOI: 10.1103/rldc-9x52

I. INTRODUCTION

The High Energy Photon Source (HEPS) is a 6 GeV fourth-generation synchrotron light source with a kilometer-scale storage ring [1,2]. Construction of HEPS started in June 2019, and the facility was successfully commissioned to 100 mA in October 2025 [3], reaching a beam current of 150 mA in March 2026. A double-frequency radio-frequency (rf) system was adopted for the storage ring, consisting of 166.6 MHz fundamental rf and 499.8 MHz active third-harmonic rf [4]. Five 166.6 MHz quarter-wave $\beta = 1$ superconducting rf (SRF) cavities were installed to provide a total accelerating voltage of 5.16 MV and rf power of 850 kW to a 200 mA electron beam. Each cavity was equipped with one fundamental power coupler (FPC) capable of delivering 200 kW of continuous-wave (cw) rf power. This power level largely exceeds those reported for existing on-cell FPCs used in transverse electromagnetic (TEM)-type SRF cavities, whose demonstrated cw power is up to 100 kW, as compared in Table I. The specified and tested FPC power levels for TEM-type SRF cavities remain below 250 kW. For elliptical SRF cavities, however, FPCs with substantially higher power ratings have been demonstrated (e.g., KEK B-Factory [5], LHC [6], and Electron-Ion Collider [7]), owing to their more favorable location on the beam pipe, where the electromagnetic fields are relatively weak rather than on the cavity wall (on-cell). Unlike these beam-pipe-mounted couplers, the FPCs for TEM-type SRF cavities must be located directly on the cavity wall to achieve the required strong coupling. This on-cell configuration exposes the coupler to the intense fields inside the cavity, creating two unique challenges: first, field-emission (FE) electrons generated inside the cavity can be deflected toward the ceramic window and cause irreversible damage; second, rf field leakage from the cavity into the coupler port can induce significant overheating at the cavity-coupler interface, even quenching the cavity. These differences

*Contact author: zhangpei@ihep.ac.cn

Published by the American Physical Society under the terms of the Creative Commons Attribution 4.0 International license. Further distribution of this work must maintain attribution to the author(s) and the published article's title, journal citation, and DOI.

TABLE I. Comparison of the specified and tested power levels of FPCs for TEM-type SRF cavities in major accelerator facilities. "QWR" stands for quarter-wave resonator, "HWR" stands for half-wave resonator, "TW" stands for traveling wave, "SW" stands for standing wave, "pk" stands for peak, and "av." stands for average.

Facility	Cavity type	Frequency (MHz)	cw or pulsed	Specified power (kW)	Tested power on stand (kW)
HEPS	QWR	166.6	cw	200	250 (TW), 150 (SW)
IFMIF [8,9]	HWR	175	cw	70	100 (TW), 100 (SW)
CiADS [10]	HWR	162.5	cw	24	30 (Partial SW)
SPIRAL-2 [11,12]	QWR	88	cw	15	10 (SW)
PIP-II [13]	Spoke	325	cw	15	12 (SW)
FRIB [14]	HWR	322	cw	5	20 (pk, TW) 4 (av., TW)
ESS [15]	Spoke	352	Pulsed (14 Hz, 2.86 ms)	250 (pk) 10 (av.)	120 (pk, SW) 4.8 (av., SW)
CSNS-II [16]	Spoke	324	Pulsed (25 Hz, 1.2 ms)	200 (pk) 6 (av.)	500 (pk., SW) 15 (av., SW)

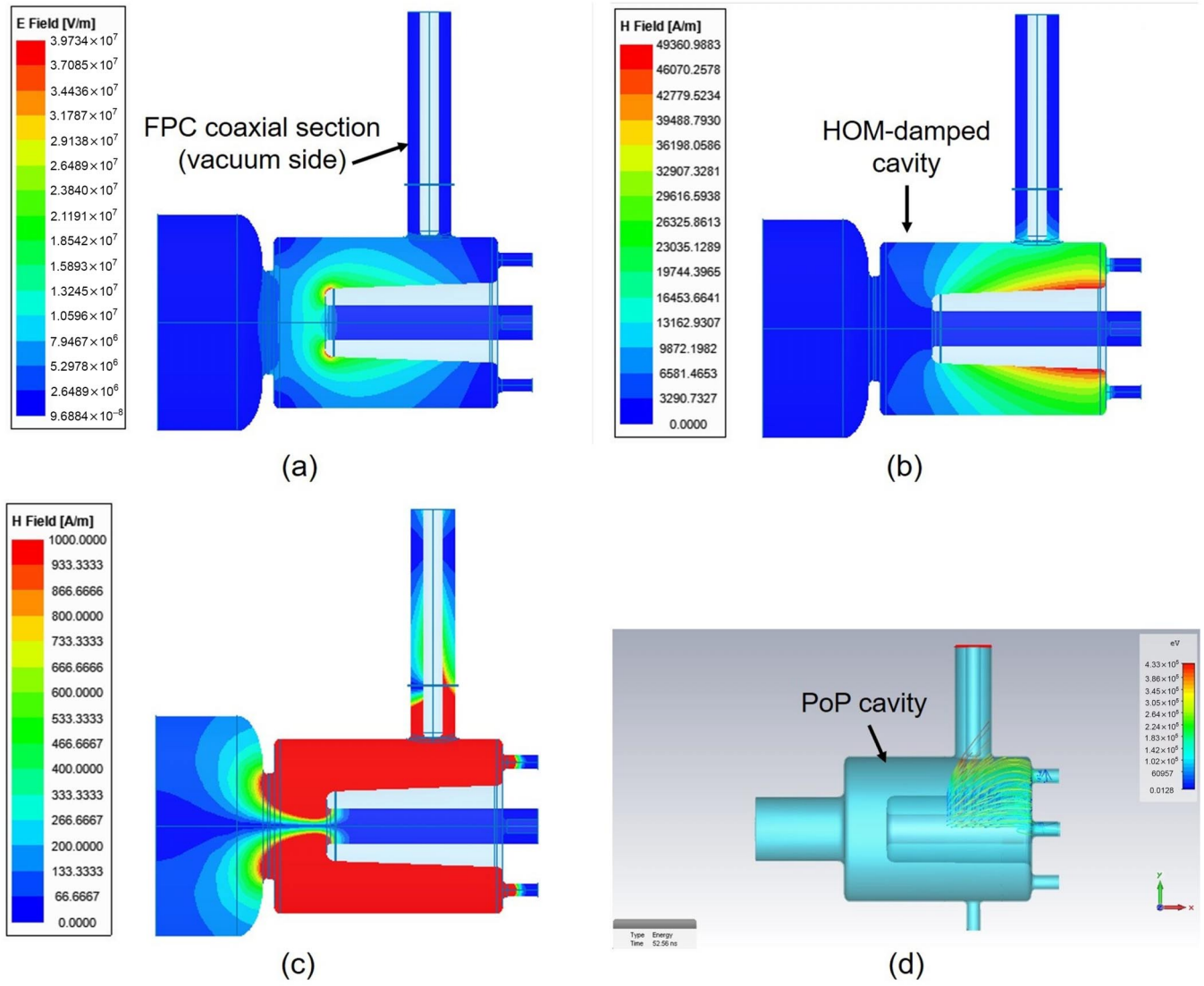


FIG. 1. Electromagnetic field distribution of the 166.6 MHz SRF cavity with an FPC at an accelerating voltage of 1.5 MV: (a) electric field; (b) magnetic field; (c) magnetic field with a reduced field scale to highlight the field leakage into the coupler port; (d) simulated field-emission electron trajectories.

substantially increase the design difficulty and limit the operating power level of the FPCs.

The design of the 166.6 MHz FPC is governed by four competing requirements: high-power handling capability (250 kW cw), low cryogenic heat load, minimal risk of FE-induced damage, and compatibility with cavity assembly in a cleanroom [17]. These requirements are inherently conflicting. High rf power operation results in significant rf losses and a large dynamic heat load, favoring a longer vacuum section and a coupler location farther from the cavity high-magnetic-field end to reduce rf field leakage into the coupler. In contrast, minimizing FE-induced ceramic-window damage, a major concern for on-cell couplers used in TEM-type cavities, requires positioning the coupler on the cavity wall close to the high-magnetic-field end, where the strong magnetic field deflects FE electrons away from the ceramic window. The selected coupler location and the corresponding electromagnetic field distribution, including the rf field leakage into the FPC, are shown in Fig. 1, together with simulated FE electron trajectories. Furthermore, the vacuum section of the single-window coupler must be assembled with the cavity in a Class-10 cleanroom. This requirement favors a compact vacuum geometry that can be accommodated within the limited cryostat envelope [18]. Consequently, the development of a high-power on-cell coupler that is simultaneously compact, thermally efficient, and robust required careful trade-offs among these competing design constraints.

The FPC design evolved from the prototype stage to series production over the past 9 years. During prototype testing at the HEPS—Test Facility (2016–2019), overheating at the cavity-coupler interface caused significant degradation of the intrinsic quality factor (Q_0) and cavity

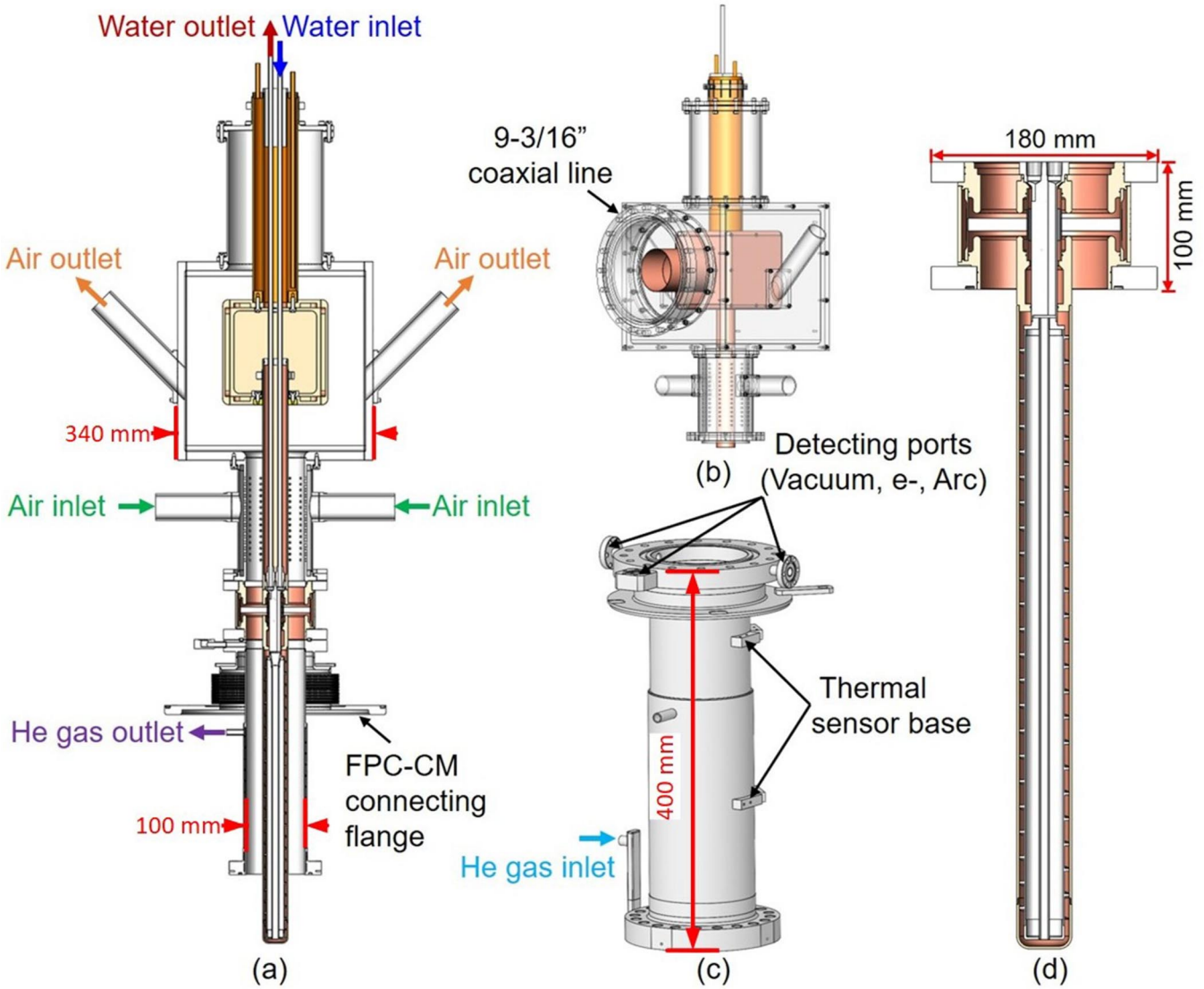


FIG. 2. The 166.6 MHz FPC assembly (a) and its main components: the T-box (b), coaxial section (c), and rf window (d).

TABLE II. Main parameters and features of the 166.6 MHz FPC. "horiz" stands for horizontal, "OD" stands for outer diameter, "L" stands for length, "Z_c" stands for characteristic impedance, "Thk" stands for thickness, "IC" stands for inner conductor, "OC" stands for outer conductor, and "SLM" stands for standard liters per minute.

Parameter		Value
Rf parameters	Frequency	166.6 MHz
	Design power	400 kW (cw)
	Tested power	250 kW (cw)
	Operation power	200 kW (cw)
	Q_{ext}	5×10^4
Features	Cavity type	Quarter-wave $\beta = 1$ SRF cavity
	FPC type	Coaxial, single window
	Window type	Coaxial disk with choke
	Coupling type	Electric
	FPC position	On cavity, horiz. mounting
Coaxial section	Dimension	OD = 100 mm, L = 400 mm
	Z_c	50 Ω
	Cu plating	Thk = 15 μm, RRR = 30
Window	Material	97.6% Al_2O_3 (Morgan, AL-300)
	Dielectric loss	0.00045 (loss tangent)
	Dimesion	OD = 120 mm, Thk = 10 mm
	Coating	TiN, Thk = 10 nm
Cooling	IC (vacuum part)	Water (3×1/ min)
	IC (air part)	Forced air (100 m^3/h)
	OC (vacuum part)	Helium gas (30 SLM)
	Window IC	Water (3l/ min)
	Inner T-box	Forced air (100 m^3/h)

quenching at the design accelerating voltage [19,20]. To address this issue, the design of Series-A (2021–2023) incorporated targeted thermal and structural modifications. Subsequent testing of the first cryomodule (CM1) confirmed the effectiveness of these improvements but revealed frosting near the rf window. This issue was eliminated in Series-B (2024–2025) through further design refinements. The final series production FPCs were validated through high-power tests on both a dedicated test stand and SRF cavities. FPCs of both series are currently operating reliably with beam at HEPS. This represents the highest cw power achieved to date by an on-cell coupler for a TEM-type SRF cavity.

This paper is organized as follows. Section II describes the design optimization of the FPCs and the evolution from prototype to Series-A and Series-B. Section III presents the high-power testing of all series FPCs on the test stand. Section IV describes the high-power testing of the series FPCs integrated with the 166.6 MHz SRF cavities during module horizontal tests, with particular emphasis on validating design modifications introduced to address issues identified in earlier test campaigns. Section V presents the performance of the installed FPCs during high-current beam operation. All series FPCs demonstrated excellent rf, vacuum, and thermal performance.

II. DESIGN OPTIMIZATION

A. Rf and mechanical design

The 166.6 MHz FPC design must simultaneously satisfy several stringent requirements: high-power transmission at 250 kW cw, strong coupling, minimal risk of field-emission-induced damage to the ceramic window, and compatibility with Class-10 cleanroom assembly. Detailed descriptions of the design are available in our previous publications [17,19]. This section summarizes the key rf and mechanical features of the final design.

The overall configuration of the FPC is shown in Fig. 2. The coupler features a 50 Ω coaxial structure with a single warm window incorporating a ceramic disk made of 97.6% alumina (Morgan AL-300). A relative dielectric constant of 9.2 and a loss tangent of 4.5×10^{-4} were used in the design simulations. To suppress secondary electron emission, the vacuum-facing surface of the ceramic is coated with a 10-nm-thick titanium nitride (TiN) layer. To achieve the required strong coupling while minimizing rf field leakage, the FPC is mounted directly on the cavity wall (on-cell). The external quality factor, Q_{ext}, is adjusted to 5×10^4 by varying the insertion depth of the inner conductor (IC). The coaxial section has an outer diameter (OD) of 100 mm and a length of 400 mm. The vacuum part

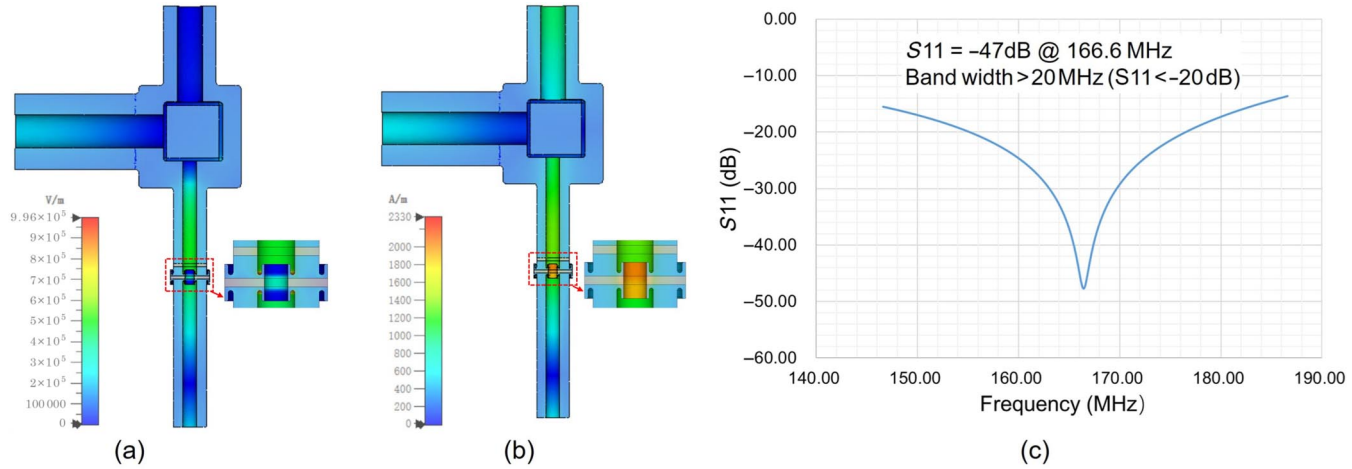


FIG. 3. Simulated electric (a) and magnetic (b) field distribution and reflection coefficient S_{11} (c) of the 166.6 MHz FPC under 400 kW cw power transmission in traveling-wave mode.

of the outer conductor is made of 316 L stainless steel plated with a 15-μm-thick copper layer (RRR ≈ 30) to minimize rf losses. The main parameters and features of the FPC are summarized in Table II.

The rf transmission characteristics of the coupler were optimized to ensure efficient power delivery. The simulated electromagnetic field distributions at 400 kW cw in traveling-wave (TW) mode are presented in Figs. 3(a) and 3(b). The simulations were performed using the CST Studio Suite [21]. The maximum electric field reads 1 MV/m and occurs at the choke structure of the rf window. This value is one-third of the breakdown field in ambient air, providing a substantial margin against arcing. The maximum magnetic field is approximately 2330 A/m, indicating that the rf losses and associated thermal load can be managed with the proposed cooling scheme. The simulated reflection coefficient, S_{11}, of the final design is shown in Fig. 3(c). At the operating frequency of 166.6 MHz, S_{11} is below −47 dB and the bandwidth over which $S_{11} < -20$ dB exceeds 20 MHz. This impedance matching enables efficient power transfer from the amplifier to the cavity over the specified operating bandwidth.

The mechanical integrity of the rf window is critical because it serves as the vacuum barrier, and the ceramic-to-metal braze joint may be a limiting component during high-power operation. Multiphysics simulations using ANSYS [22] were performed to evaluate the thermal and mechanical behavior of the window under 400 kW cw rf transmission in TW mode, corresponding to twice the nominal operating power of 200 kW. As shown in Fig. 4, the maximum temperature reaches 319 K

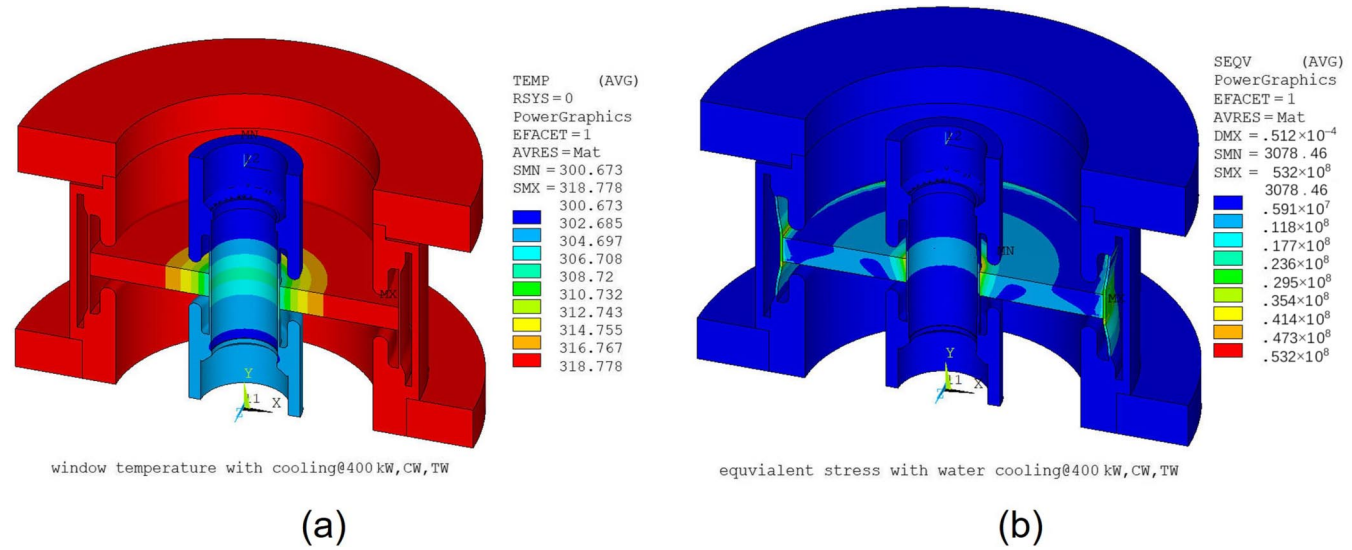


FIG. 4. Simulated temperature (a) and thermal stress (b) of the rf window under 400 kW cw power transmission in traveling-wave mode.

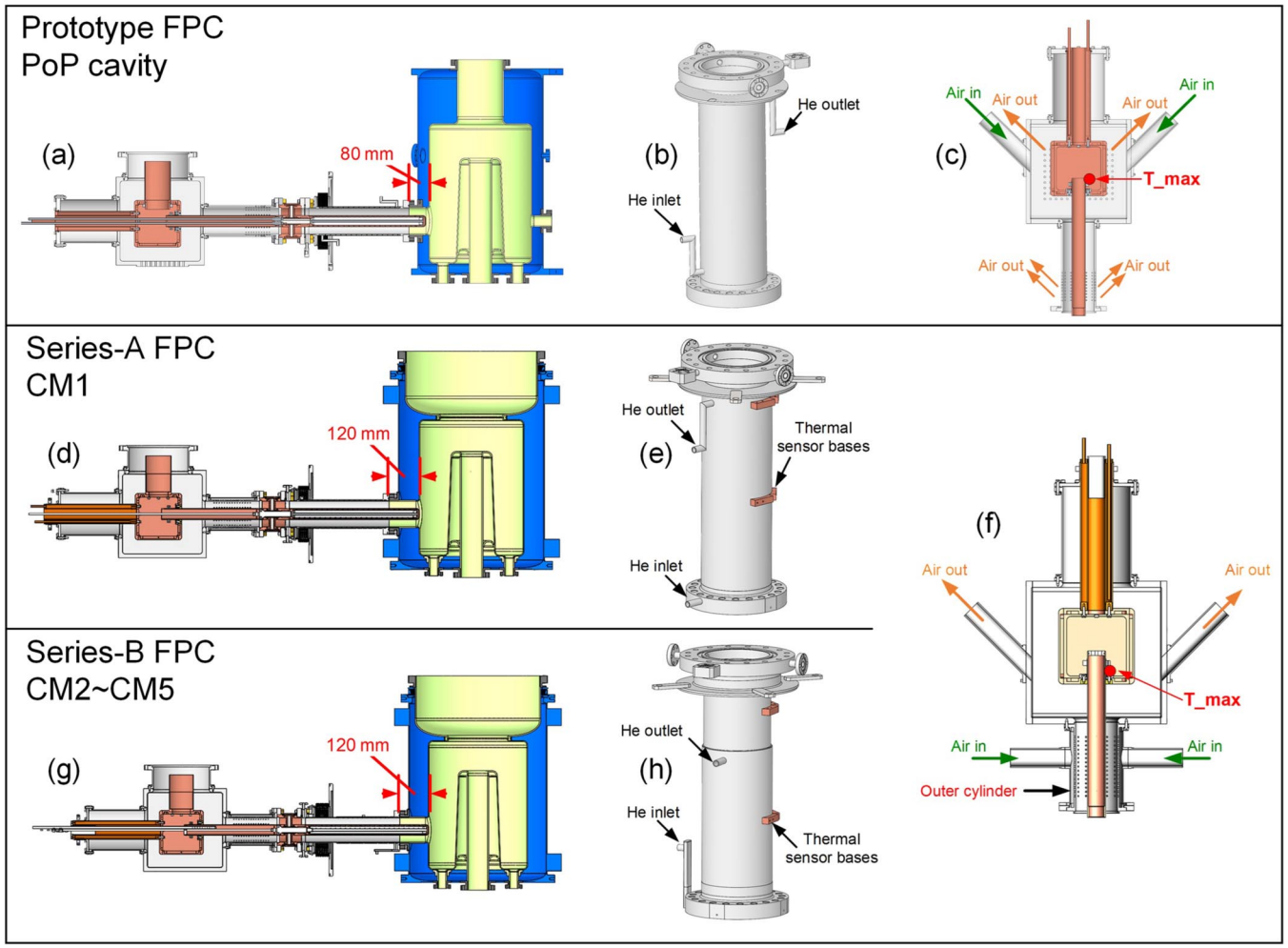


FIG. 5. Design evolution of the 166.6 MHz FPC: cavity-coupler assemblies of the prototype (a), Series-A (d) and Series-B (g); outer conductors of the prototype (b), Series-A (e) and Series-B (h); air-side sections with their cooling configurations of the prototype (c) and Series-A and Series-B (f).

(approximately 46°C) in the ceramic near the outer window. The resulting maximum thermal stress is 53.2 MPa and occurs at the braze joint between the ceramic and the outer conductor. This stress is well below the specified flexural strength of the alumina ceramic (296 MPa), indicating sufficient cooling. These results confirm a robust window design for high-power cw operation.

B. From prototype to Series-A

Two prototype FPCs were developed for the 166.6 MHz proof-of-principle (PoP) SRF cavities between 2016 and 2019 [20,23,24]. They were validated through high-power tests both on a test stand at room temperature and on the cavity installed in a test cryomodule at cryogenic temperatures [17]. Both temperature and cryogenic heat-load measurements revealed overheating in the cavity-coupler interface region. This issue resulted in significant Q_0 degradation and ultimately caused cavity quenching at the design accelerating voltage of 1.5 MV during the horizontal test. This overheating is a direct consequence of the on-cell configuration: the strong magnetic field inside the cavity leaks into the coupler port and deposits significant rf power on the copper-plated stainless-steel surface of the FPC's outer conductor. This heating is expected to be much less severe if the coupler is mounted on the beam pipe. Based on detailed rf-thermal simulations of the coupler-cavity system, the length of the niobium coupler port was increased from 80 to 120 mm to ensure sufficient attenuation of the rf field before it enters the nonsuperconducting coupler, as shown in Figs. 5(a) and 5(d). Meanwhile, the inlet of the helium-gas cooling pipe was relocated from the outer-conductor sidewall to the cold flange to further reduce the temperature rise in the cavity-coupler interface region. Simulated temperature distributions of the cavity-coupler interface for these designs are shown in Figs. 6(a) and 6(b), predicting that the maximum temperature is significantly reduced from 32.3 to 17.7 K. In addition, several dedicated thermal sensor mounting bases were incorporated into the

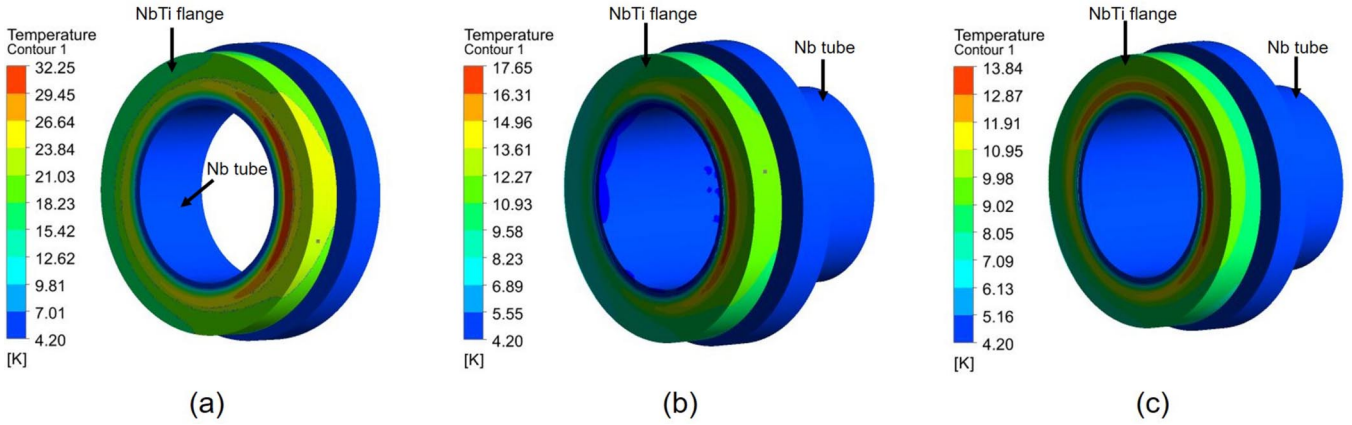


FIG. 6. Simulated temperature distribution of the cavity-coupler interface at a cavity voltage of 1.5 MV: (a) prototype, (b) Series-A, and (c) Series-B.

outer conductor to improve the accuracy of temperature measurements, as illustrated in Figs. 5(b) and 5(e). Further details of the overheating mechanism and the corresponding mitigation measures can be found in Ref. [19].

In addition, the measured maximum temperature rise, observed at the inner T-box (denoted as "T_max" in Figs. 5(c) and 5(f)), reached 1.6°C per 10 kW increase in rf power, nearly twice the simulated value of 0.8°C per 10 kW. In order to reduce the temperature rise of the air-side IC, an improved cooling scheme inspired by jet impingement was developed. Figures 5(c) and 5(f) show the prototype and improved air-cooling configurations of the IC, respectively. In the new design, the airflow direction is reversed compared to the original configuration, allowing the incoming cool air to first reach the IC section adjacent to the ceramic window. Furthermore, the perforated outer conductor is enclosed by an additional tube equipped with two air-inlet ports. The tube also serves

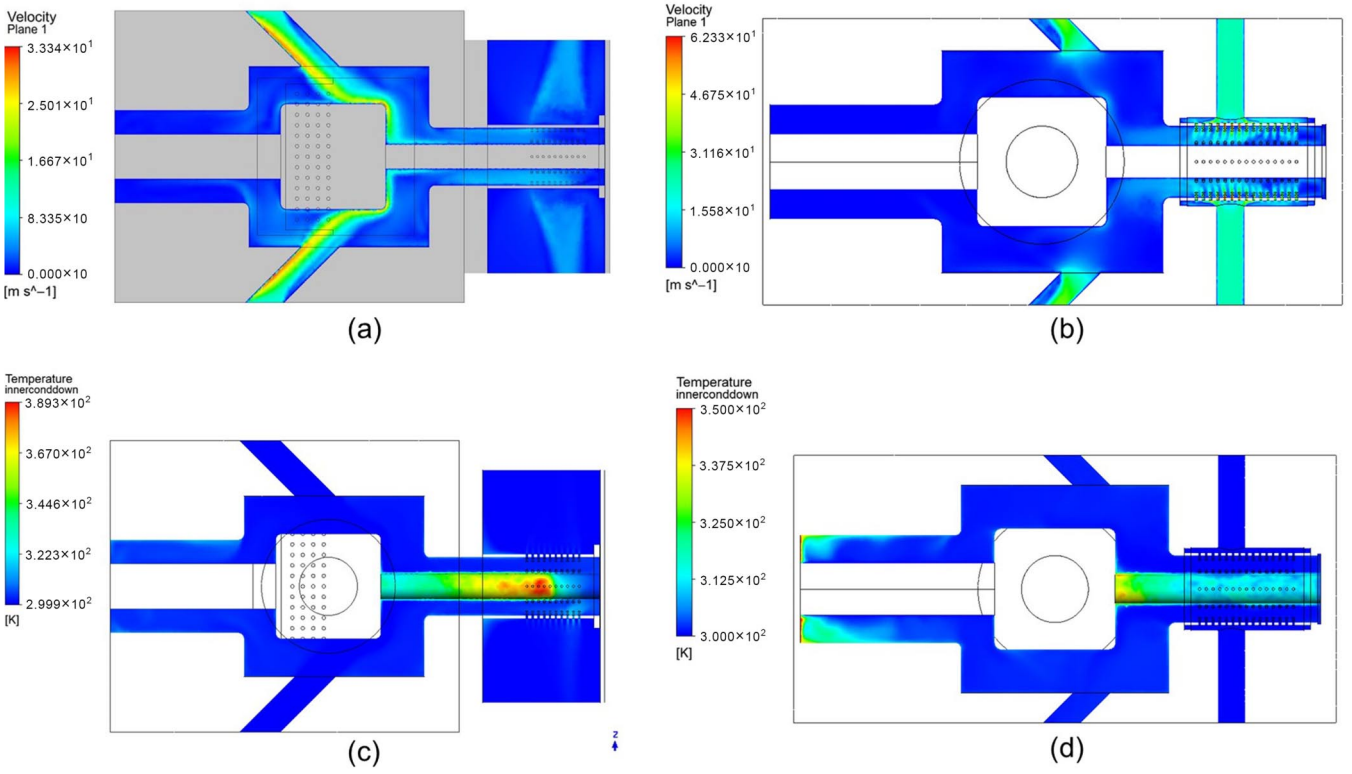


FIG. 7. Simulated airflow velocity (a),(b) and temperature distribution (c),(d) of the air-side section for the original cooling configuration (a),(c) and the improved cooling configuration (b),(d) under 250 kW cw rf power transmission in traveling-wave operation.

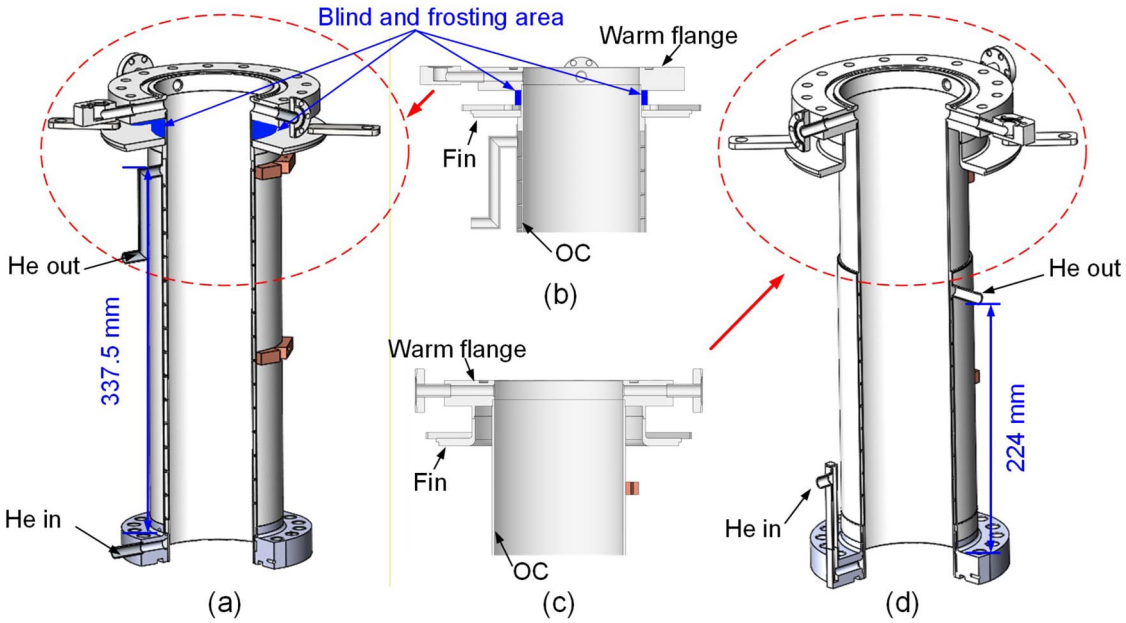


FIG. 8. Modifications to eliminate frosting: (a) outer conductor of the Series-A FPC (CM1), with the frosting region highlighted in blue; (b) enlarged view of the fin structure of the Series-A FPC; (c) enlarged view of the fin structure of the Series-B FPC; (d) outer conductor of the Series-B FPC (CM2–CM5).

as a microwave shield. The impinging airflow generated through the perforations is expected to significantly enhance the heat-exchange efficiency. The effectiveness of this design was evaluated through coupled rf-fluid-thermal simulations using the ANSYS Workbench software suite. Figure 7 shows the simulated airflow velocity and temperature distributions of the air-side section before and after implementation of the improved cooling scheme under 250 kW cw rf power transmission in TW operation. For a force-air flow rate of 100 m^3/h, the maximum airflow velocity increased from 33 to 62 m/s. Consequently, the predicted maximum temperature rise of the IC air section decreased from 116°C to 77°C at an ambient temperature of 27°C.

All of the modifications described above were implemented in the first Higher Order Mode (HOM)-damped 166.6 MHz SRF module (CM1) [25–27]. This iteration marked the first design upgrade from the prototype to the Series-A.

C. From Series-A to Series-B

Two Series-A FPCs were manufactured and high-power tested, with one installed on CM1. The subsequent horizontal test of CM1 demonstrated that the overheating issue had been effectively mitigated, as will be discussed in Sec. IV. However, a new issue emerged: despite wrapping heating tape around the window-OC connecting flange, frosting was still observed near the window and the

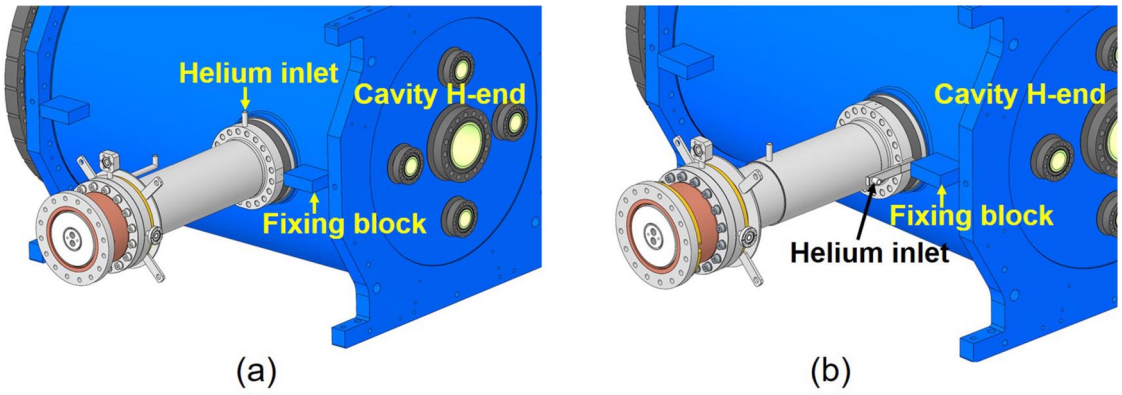


FIG. 9. Structure and location of the helium inlet pipe for FPC outer-conductor cooling: (a) Series-A FPC (CM1); (b) Series-B FPC (CM2 to CM5).

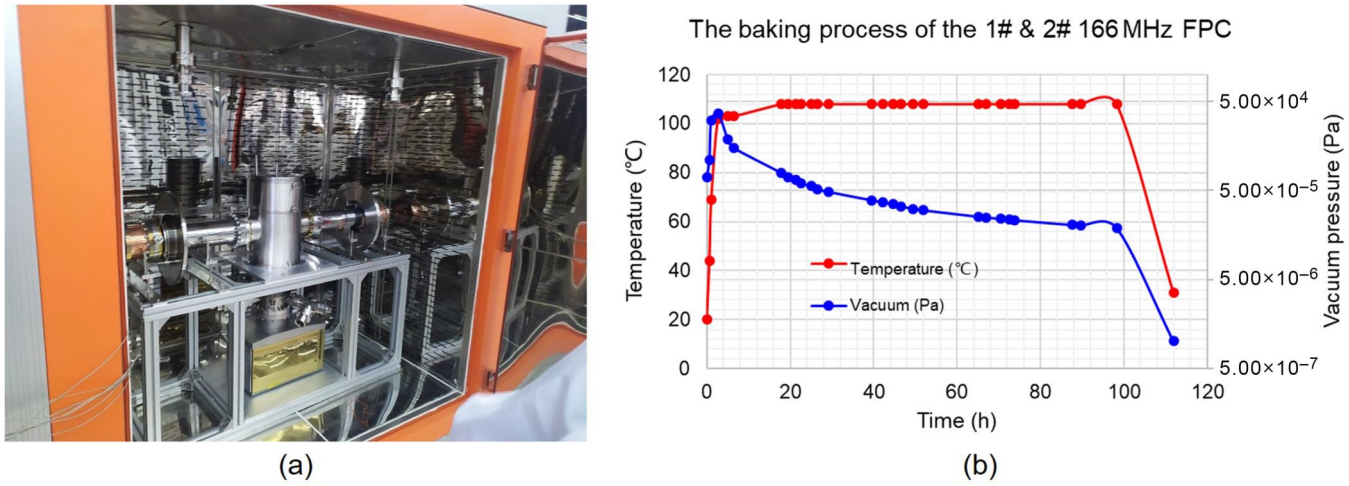


FIG. 10. (a) Baking oven for the FPCs, (b) temperature, and vacuum pressure during a typical baking process.

bellows of the coupler-cryostat connecting flange. These regions were inaccessible to the heating tape because of spatial constraints [Fig. 8(a)], posing a risk of vacuum leaks during long-term operation. To address the frosting issue, increasing the heating-tape power was initially attempted. However, complete elimination of the frosting was not achieved because the heating tape could not directly cover the affected regions in the existing design. This thermally inaccessible region, the "blind area," was subsequently eliminated by relocating the fin structure from the OC sidewall to the bottom of the warm flange, as shown in Figs. 8(b) and 8(c). Furthermore, the outlet of the helium-gas cooling pipe was moved 113.5 mm away from the frosting region, as shown in Figs. 8(a) and 8(d). Simulations predicted that this modification would reduce the required heating-tape power by approximately 50% to prevent frosting.

In addition, the gas helium inlet pipe was relocated closer to the cavity high-magnetic-field end to ensure that the cold helium gas first reaches the region with the highest thermal load, thereby further reducing the temperature rise in the coupler-cavity interface region. As shown in Fig. 6(c), the maximum temperature in this region is further reduced to 13.8 K. To avoid interference with the cavity fixing block, the helium inlet pipe was bent by 90°. The modification is illustrated in Figs. 9(a) and 9(b).

These modifications were incorporated into the final design (Series-B) of the FPCs and installed in the subsequent SRF modules. The effectiveness of these design changes was then evaluated in the horizontal tests of CM2–CM5, as detailed in Sec. IV.

III. ON-STAND HIGH-POWER TESTS

Before being integrated with the cavity, each FPC must undergo high-power conditioning on a dedicated test stand at room temperature to remove residual gases, dust, and

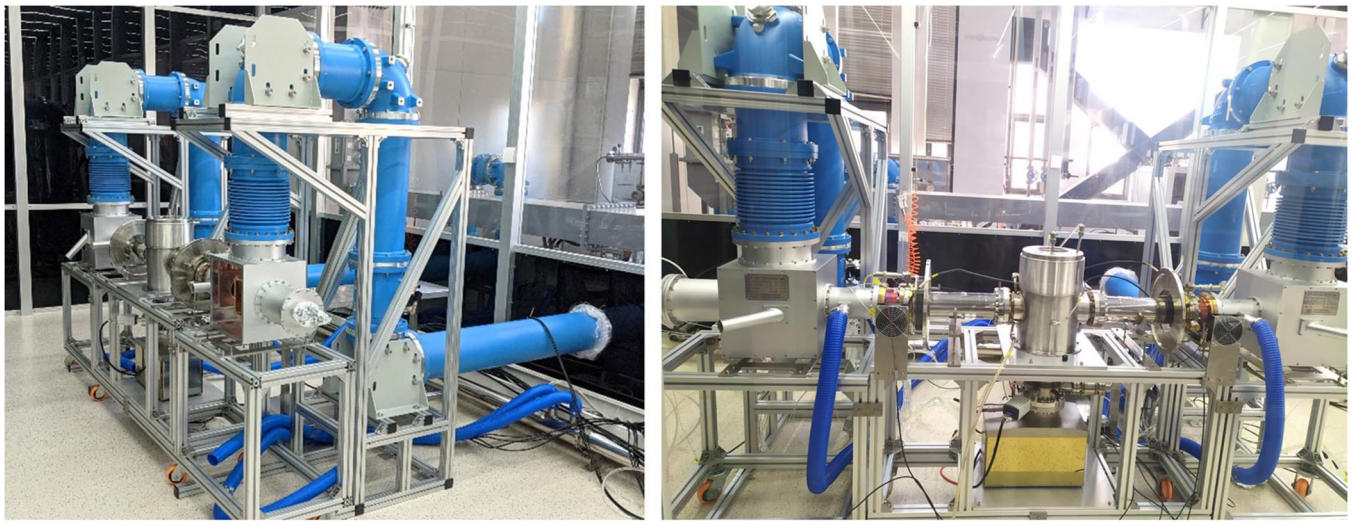


FIG. 11. On-stand high-power test setup for the FPCs in a Class-100 cleanroom.

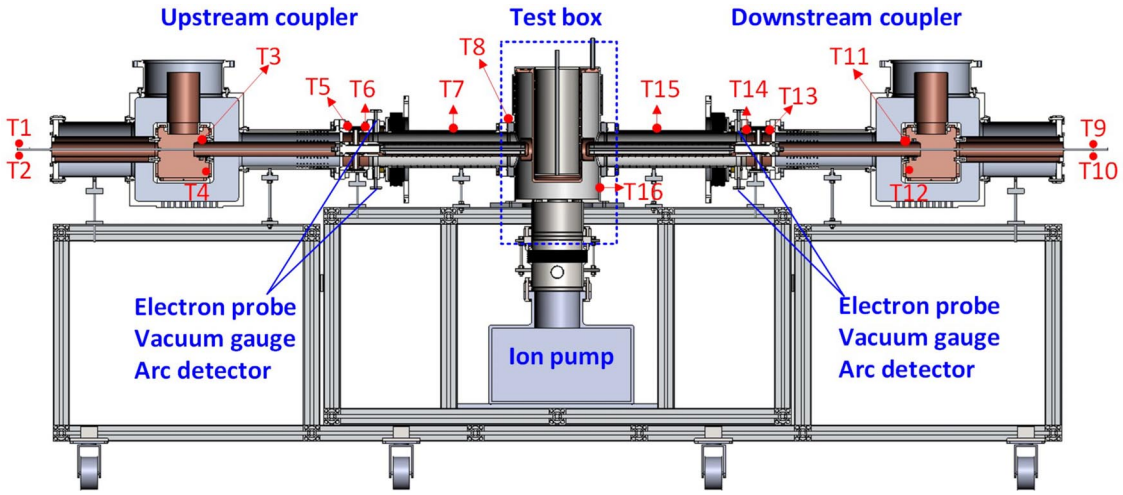


FIG. 12. Temperature sensor locations during the on-stand test.

particulates, thereby minimizing the risk of cavity contamination. In addition, comprehensive rf, vacuum, and thermal validation of the coupler performance is essential. To this end, all FPCs, including two Series-A and eight Series-B units, were tested on the test stand.

A. Preparation and setup

The preparation process, including ultrapure water cleaning, assembly, and baking, followed the same procedure as that used for the prototype couplers [17]. Nevertheless, two process improvements were introduced to enhance the coupler performance. First, a specially designed baking oven [Fig. 10(a)] equipped with vacuum pumping, temperature control, and nitrogen-gas filling capabilities was developed to bake the entire coupler-bench system at 110°C for more than 48 h [Fig. 10(b)]. This approach prevented surface oxidation of the coupler while improving the effectiveness of the baking process. More importantly, the oven door could be opened directly inside the cleanroom, allowing the entire baking process to be performed in a Class-100 cleanroom environment. Second, unlike the prototype FPCs, for which only cleaning and assembly were performed in a cleanroom, the high-power conditioning of the series FPCs was also conducted in the cleanroom, with the setup shown in Fig. 11 inside a Class-100 cleanroom environment. Furthermore, both pre-test assembly and post-test disassembly were performed in the same Class-10 cleanroom used for SRF cavity assembly. Therefore, the entire on-stand test sequence was conducted under cleanroom conditions. This modification significantly improved cleanliness and reduced the risk of cavity contamination, which is particularly important for TEM-type SRF cavities equipped with on-cell FPCs.

The upstream coupler was connected to a 166.6 MHz 260 kW solid-state amplifier through a 9-3/16-inch rigid coaxial transmission line, while the downstream coupler was terminated either by a 300 kW rf load for TW tests or by a variable short circuit for standing-wave (SW) tests.

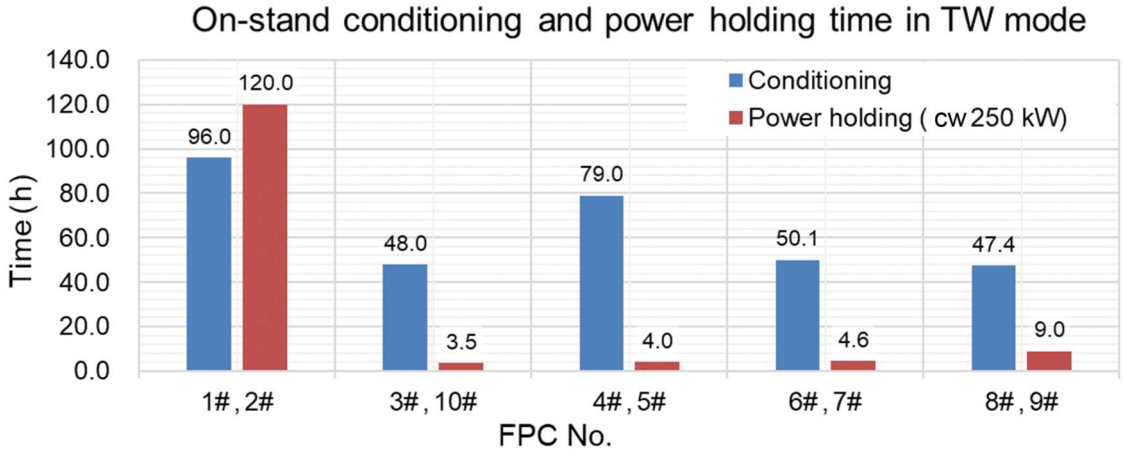


FIG. 13. Duration of the initial on-stand conditioning and subsequent 250 kW cw power-holding test in traveling-wave mode.

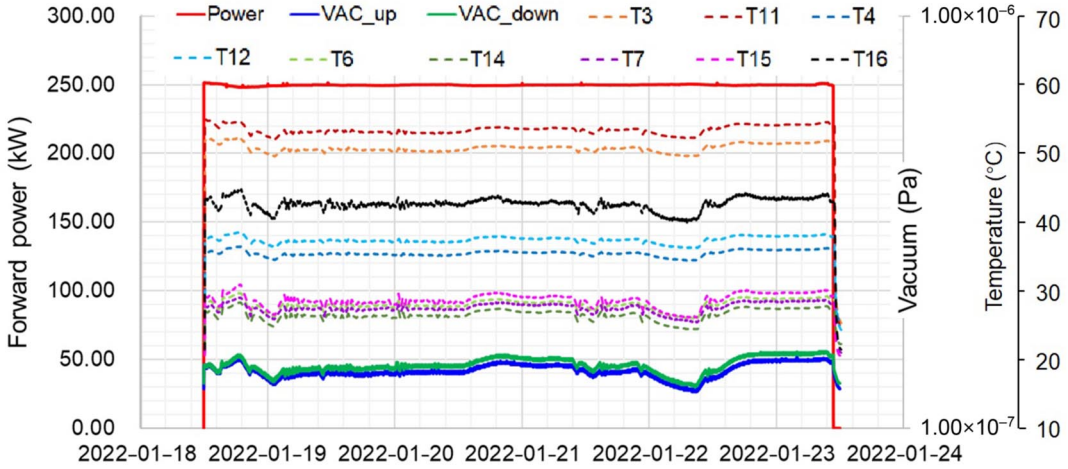


FIG. 14. Vacuum pressure and temperature records of the two Series-A FPCs (1#, 2#) during the 120 h power-holding test at 250 kW cw in traveling-wave mode on the test stand.

B. On-stand test results

The conditioning was initially conducted in pulsed mode at a fixed repetition rate of 1 kHz with the pulse width progressively increased from 1 to 5, 10, 100, and 200 μs before transitioning to cw. During conditioning, the FPCs were protected by an interlock system against vacuum degradation, arc discharges, and overheating. Sixteen thermocouples were installed at critical locations on the couplers and the test box to monitor the temperature rise, as shown in Fig. 12. The entire conditioning process was performed automatically using software developed within the Experimental Physics and Industrial Control System (EPICS) framework [28]. The test results are presented below in terms of conditioning procedure, thermal performance, and multipacting behavior, providing a comprehensive validation of the series FPC design.

The initial conditioning of the first two FPCs (1#, 2#) in TW mode required the longest duration, taking 96 h to reach 250 kW cw operation, including the time required for commissioning and debugging of the test system. In contrast, the subsequent eight FPCs reached 250 kW cw in a shorter time, benefiting from improved cleanliness and the automated conditioning system. After the initial conditioning, all FPCs were maintained at 250 kW cw to verify the stability of high-power operation. For the first two FPCs, the power-holding test lasted 120 h. Owing to the tight project schedule, the subsequent eight FPCs were maintained at 250 kW cw for only 3.5–9 h. Figure 13 summarizes the durations of the initial TW conditioning and the subsequent power-holding tests. Finally, each FPC was further conditioned in SW mode up to 150 kW cw. During the SW conditioning, the position of the variable short circuit was adjusted in increments of one-sixteenth of

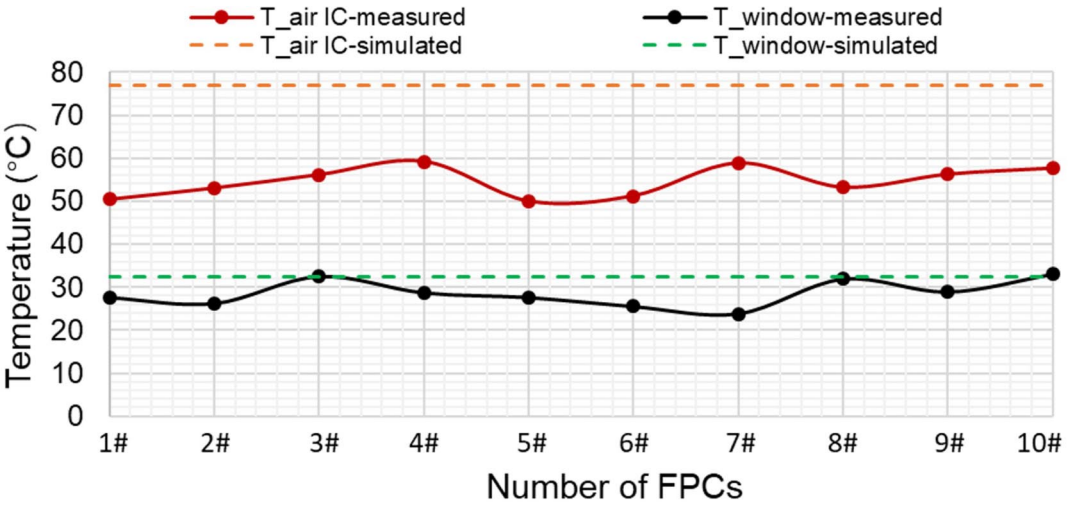


FIG. 15. Comparison of the simulated and measured maximum temperatures and ceramic-window temperatures during the 250 kW cw power-holding test on the test stand.

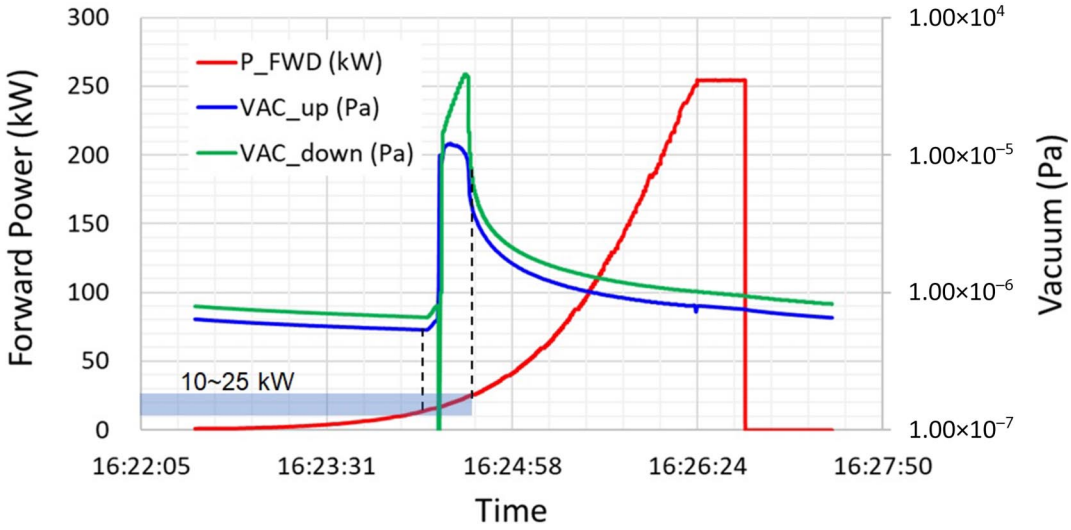


FIG. 16. Hard multipacting barriers observed during rf power ramping in traveling-wave mode after the initial on-stand traveling-wave conditioning.

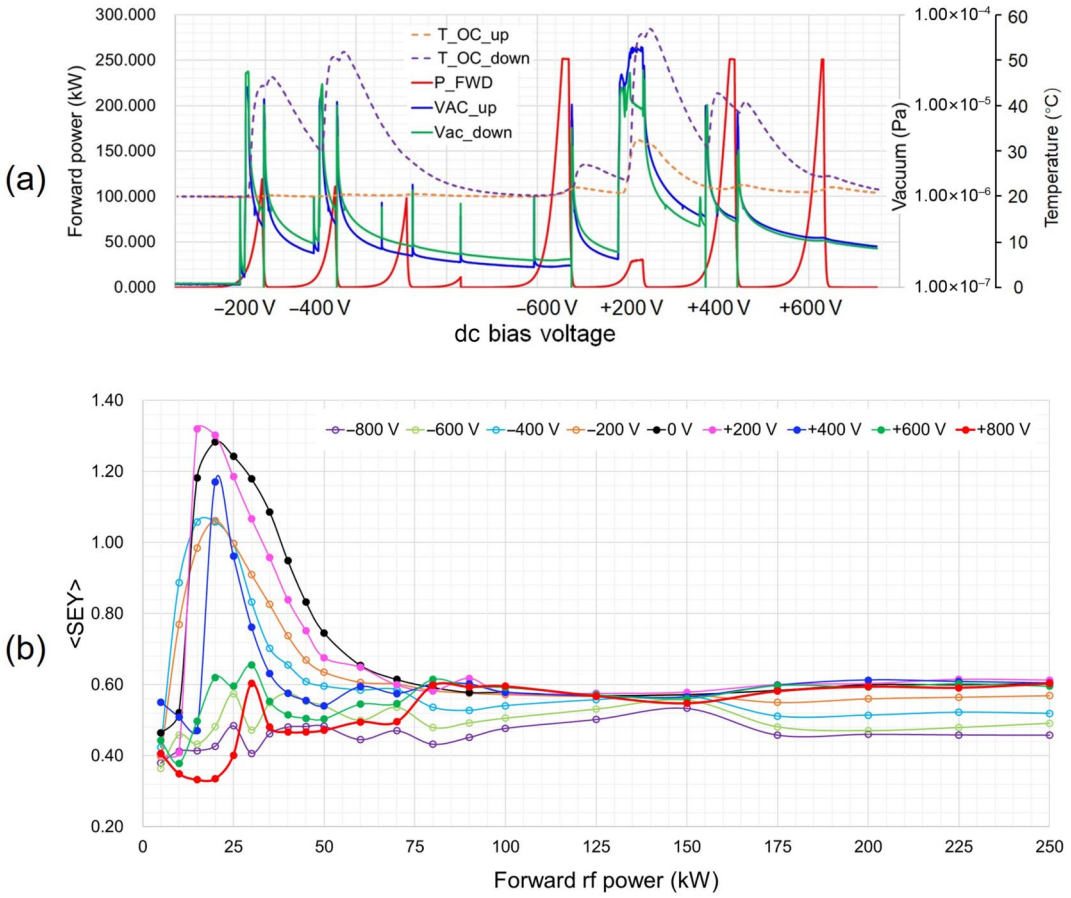


FIG. 17. On-stand traveling-wave conditioning with different dc-bias voltages:(a) test results; (b) simulation results. ⟨SEY⟩ stands for normalized secondary electron yield.

the 166.6 MHz wavelength (112.5 mm) to ensure that all rf surfaces along the coupler were adequately conditioned.

All FPCs exhibited excellent rf, vacuum, and thermal performances during the power-holding tests. Taking the two Series-A FPCs (1#, 2#) as an example, the vacuum pressure remained below 1.4×10^{-7} Pa throughout the test. The maximum measured temperatures were 50.4°C (T3) and 53.0°C (T11), both located at the inner conductor of the air-side section inside the inner T-box, as shown in Fig. 14. The measured maximum and ceramic-window temperatures during the 250 kW cw power-holding tests were compared with the corresponding simulated values, as shown in Fig. 15. The measured window temperature agrees well with the simulation, while the measured maximum temperature is significantly lower than the predicted value, further demonstrating the effectiveness of the improved cooling scheme.

During the initial TW conditioning, multipacting was observed at incident powers between 10 and 50 kW, in good agreement with the simulation results [17]. In addition, hard multipacting barriers were identified between 10 and 25 kW. These barriers were manifested by a pronounced deterioration of the vacuum pressure when the rf power was ramped to 250 kW cw after the initial conditioning, as shown in Fig. 16.

To suppress the hard multipacting barriers observed after the initial TW conditioning, a dc-bias voltage was applied, and its value was varied to determine the optimal operating setting. The bias voltage was scanned from −200 to −600 V and then from +200 to +600 V in steps of 200 V. A bias voltage of +600 V or higher was found to effectively suppress hard multipacting. In contrast, multipacting-induced outgassing was observed at bias voltages ranging from −600 to +400 V, as shown in Fig. 17(a). This observation is consistent with the simulation results in Fig. 17(b) and may be attributed to the excitation of new multipacting zones or insufficient suppression of the hard multipacting barriers at certain bias voltages. The severity of multipacting in the simulations is characterized by the normalized secondary electron yield, ⟨SEY⟩, defined as the ratio of the total number of secondary electrons produced to the total number of electron impacts. Based on both simulation and test results, a bias voltage of +800 V was selected for subsequent beam operation. In addition to outgassing, multipacting also caused overheating of the outer conductors during the initial conditioning, with the temperature increasing from approximately 20°C to 50°C within several minutes. This anomalous heating diminished rapidly after effective conditioning. Furthermore, owing to the controlled cleanroom preparation and conditioning procedures, no arc discharges were observed during the on-stand conditioning of any series FPCs.

IV. ON-CAVITY HIGH-POWER TESTS

Following the on-stand high-power tests, one Series-A FPC was installed on the first 166.6 MHz SRF module (CM1) and four Series-B FPCs were integrated with the subsequent four modules (CM2–CM5), respectively, and participated in the corresponding cryomodule horizontal tests. This section presents the on-cavity high-power tests of these FPCs, with particular emphasis on evaluating and validating the successive design improvements.

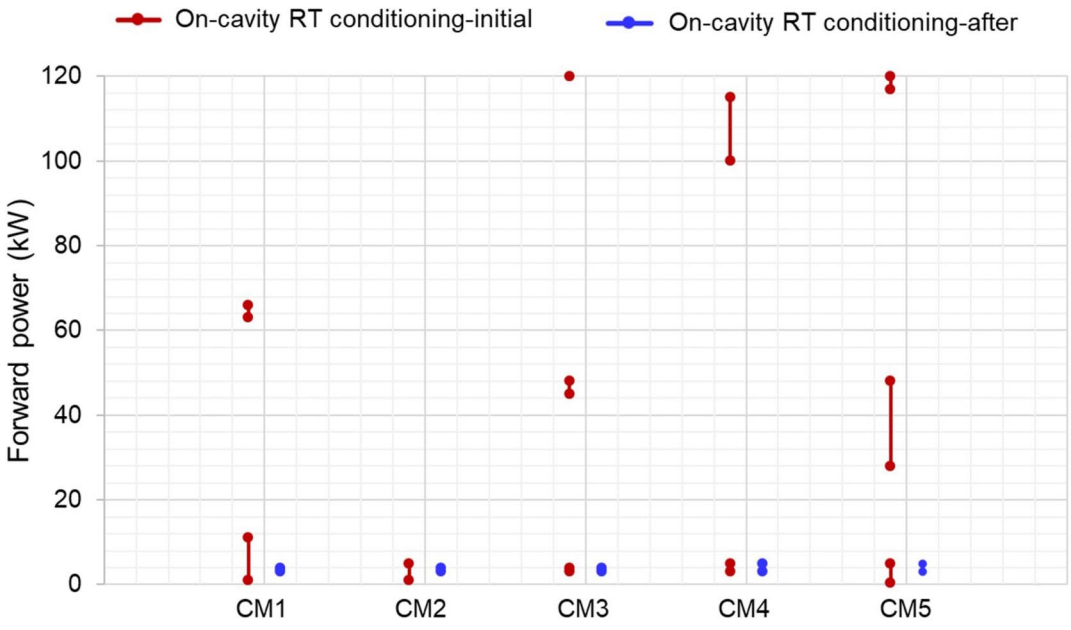


FIG. 18. Outgassing bands observed during the initial and final stages of the on-cavity room-temperature conditioning in standing-wave mode. "RT" stands for room temperature.

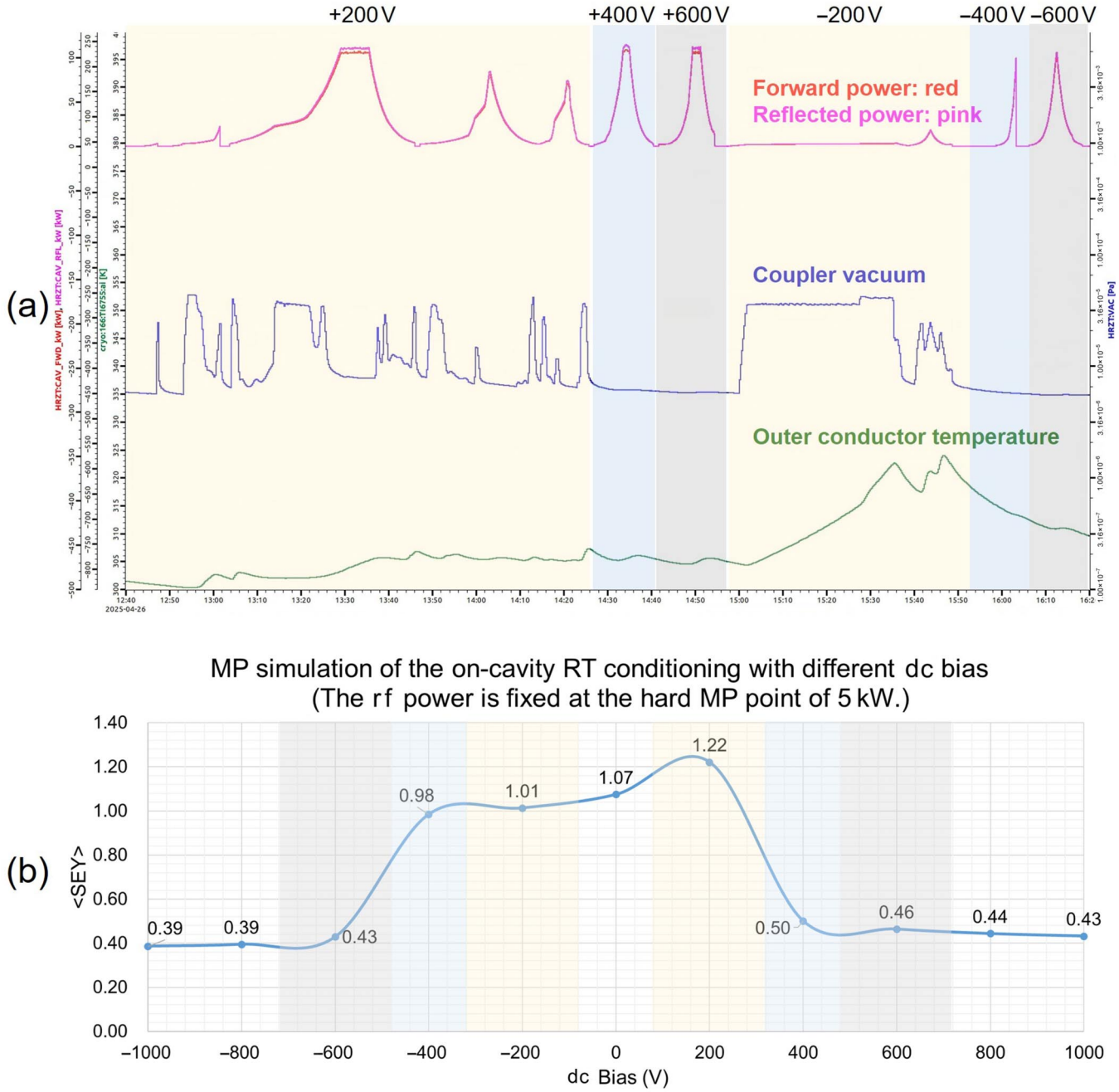


FIG. 19. Room-temperature on-cavity conditioning of the FPC in standing-wave mode with different dc bias: (a) test results; (b) simulation results with rf power fixed at 5 kW, corresponding to the hard multipacting point. ⟨SEY⟩ stands for normalized secondary electron yield.

A. Rf conditioning

Because the superconducting cavity acts as an efficient cryopump at cryogenic temperatures, each FPC was thoroughly outgassed by rf conditioning prior to module cooldown to prevent cavity performance degradation from gas absorption on the cold rf surface. The rf frequency was detuned by 400 kHz (approximately 10 times the cavity bandwidth) from the cavity resonance to prevent rf field buildup inside the cavity. The power was limited to 120 kW in SW mode. During the initial conditioning, several outgassing bands were observed over a wide range of rf power levels. Fortunately, all outgassing bands above 20 kW were successfully eliminated after conditioning, as shown in Fig. 18. However, each FPC exhibited a persistent outgassing band between 3 and 5 kW (SW), corresponding to approximately one fourth of the simulated hard multipacting band of 10–25 kW in TW mode [17].

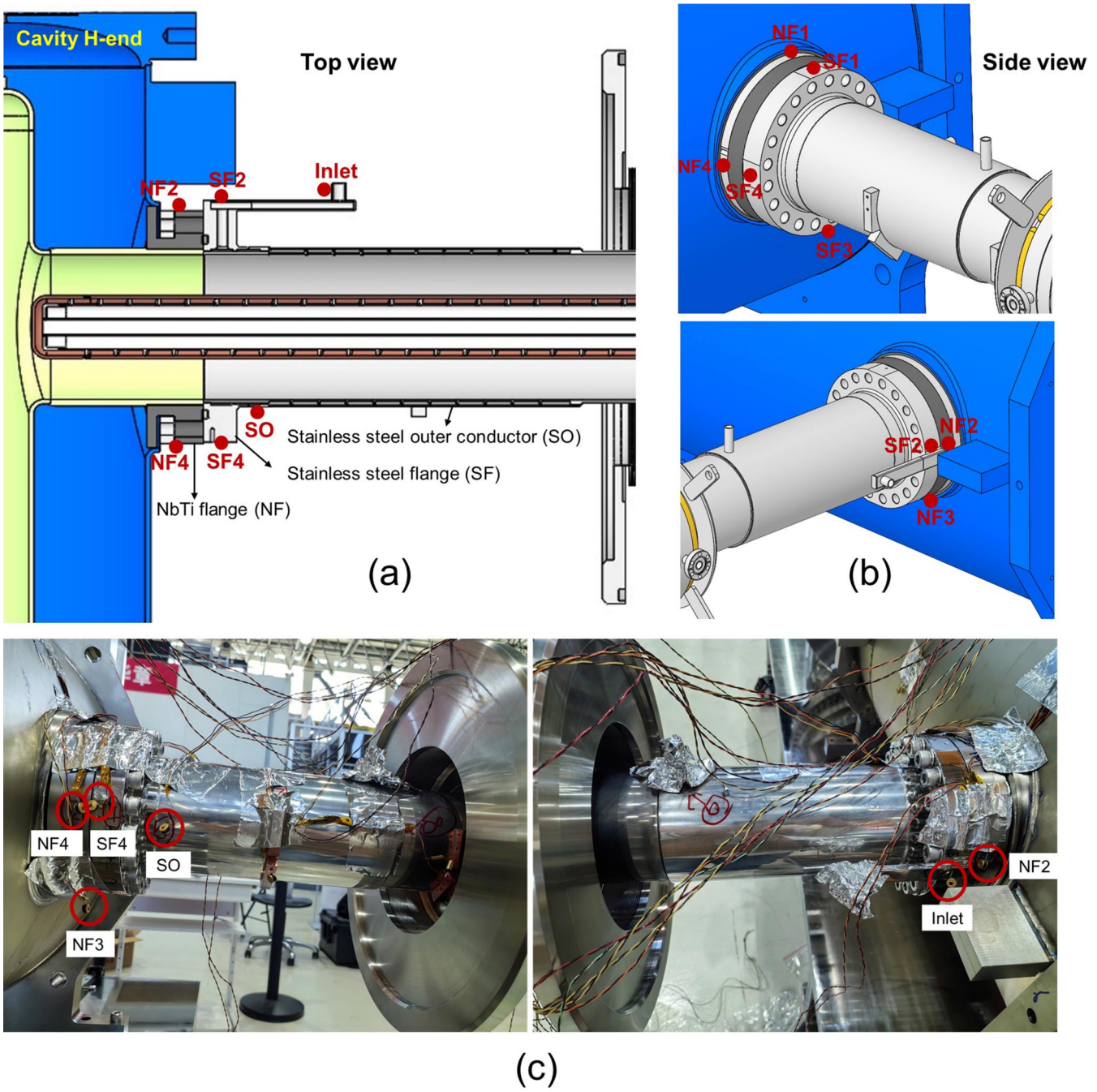


FIG. 20. Temperature sensor locations in the cavity-coupler interface region: top view (a) and side view (b) of all temperature-monitoring points considered in the design; (c) installation of the six Cernox sensors in the final two SRF modules (CM4 and CM5).

To ensure sufficient outgassing from the FPCs, dc-bias conditioning was performed after the standard rf conditioning to intentionally induce, rather than suppress, multipacting. Significant multipacting-induced outgassing was observed when a dc-bias voltage of ± 200 V was applied between the inner and outer conductors of the FPC, as shown in Fig. 19(a). This observation is consistent with the simulation results shown in Fig. 19(b), where the rf power was fixed at 5 kW, corresponding to the hard multipacting point. However, at a bias voltage of -200 V, significant heating of the outer conductor occurred due to electron bombardment associated with multipacting. In order to protect the cryogenic temperature sensors from overheating, conditioning at -200 V was performed using only pulsed rf power with a low duty factor, while the average rf power was monitored using cw power meters.

Once the module was cooled to 4.2 K, the cavity was tuned to the target resonant frequency of 166.6 MHz,

TABLE III. Comparison of the simulated and measured temperatures at sensor SO and the corresponding 4.2 K cryogenic heat load for the PoP module (1.1 MV) and CM1 equipped with the Series-A FPC (1.2 MV). The helium-gas flow rate was 14 SLM in both cases.

	PoP (1.1 MV) (He flow: 14 SLM)		Series-A (1.2 MV) (He flow: 14 SLM)	
Parameters	Sim.	Meas.	Sim.	Meas.
Temperature at SO (K)	26.0	35.0	10.7	14.2
Heat load at 4.2 K (W)	7.7	11.1	1.8	3.0

followed by rf conditioning of both the cavity and the FPC. Continuous optimization of the pulse repetition rate and pulse width to maintain the vacuum pressure near the interlock threshold proved essential for efficiently eliminating the alternating outgassing bands observed in both the cavity and the coupler. It should also be noted that the minimum pulse width must exceed the cavity field buildup time to effectively condition multipacting-induced outgassing within the cavity. In the present system, this value is 96 μs ($\tau = Q_{\text{ext}}/(\pi \times \text{Frequency}) = 5 \times 10^4/(\pi \times 166.6\ \text{MHz}) \approx 96\ \mu\text{s}$). Accordingly, cavity multipacting conditioning was initiated with a pulse width of 150 μs at a fixed repetition rate of 0.1 kHz. Depending primarily on the vacuum surface condition of the cavity and the FPC, 10–26 h were required to reach an accelerating voltage of 1.6 MV.

B. On-cavity test results

After the rf conditioning at 4.2 K, the high-power performance of the cavity system was evaluated over a range of accelerating voltages, focusing on the cryogenic heat load, as quantified by the quality factor Q_0. For the FPCs, since successive design improvements were introduced to mitigate the overheating issues, the evaluation focused on their thermal performance under high-voltage operation, particularly the temperature rise in the cavity-coupler interface region and the cryogenic heat load introduced by the couplers. Accordingly, several temperature sensors were installed in the cavity-coupler interface region and at the cold end of the outer conductor near the cavity side. The locations of all temperature-monitoring points are shown in Figs. 20(a) and 20(b). During the test campaign, only six Cernox® sensors were available. Their installation locations were adjusted and optimized among different modules according to measurement objectives. The sensor arrangement adopted for the final two SRF modules (CM4 and CM5) is shown in Fig. 20(c). All sensors were mounted on custom-designed bases to ensure reliable temperature measurements.

1. Series-A

As described in Sec. II, two modifications were introduced in the Series-A FPCs to mitigate the overheating observed during the horizontal test of the PoP cavity: a 40 mm extension of the niobium coupler port and relocation of the helium-gas cooling inlet for the outer conductor. With these modifications, both the temperature rise in the cavity-coupler interface region and the 4.2 K heat load contributed by the coupler were expected to be substantially reduced for CM1. Table III summarizes the

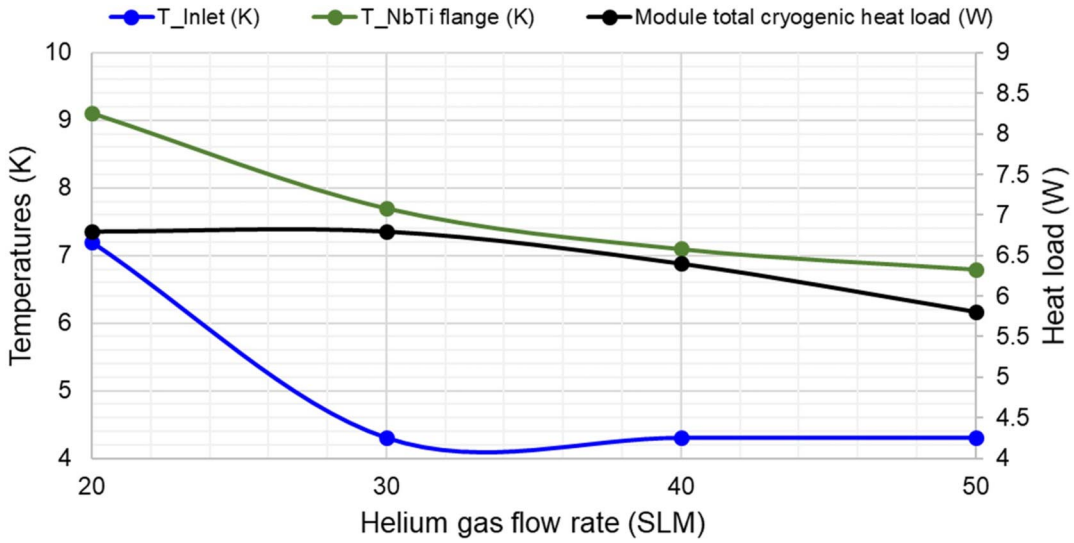


FIG. 21. Variation of the temperature rise and total cryogenic heat load with helium-gas flow rate at a cavity voltage of 1.2 MV for Series-A FPC on CM1.

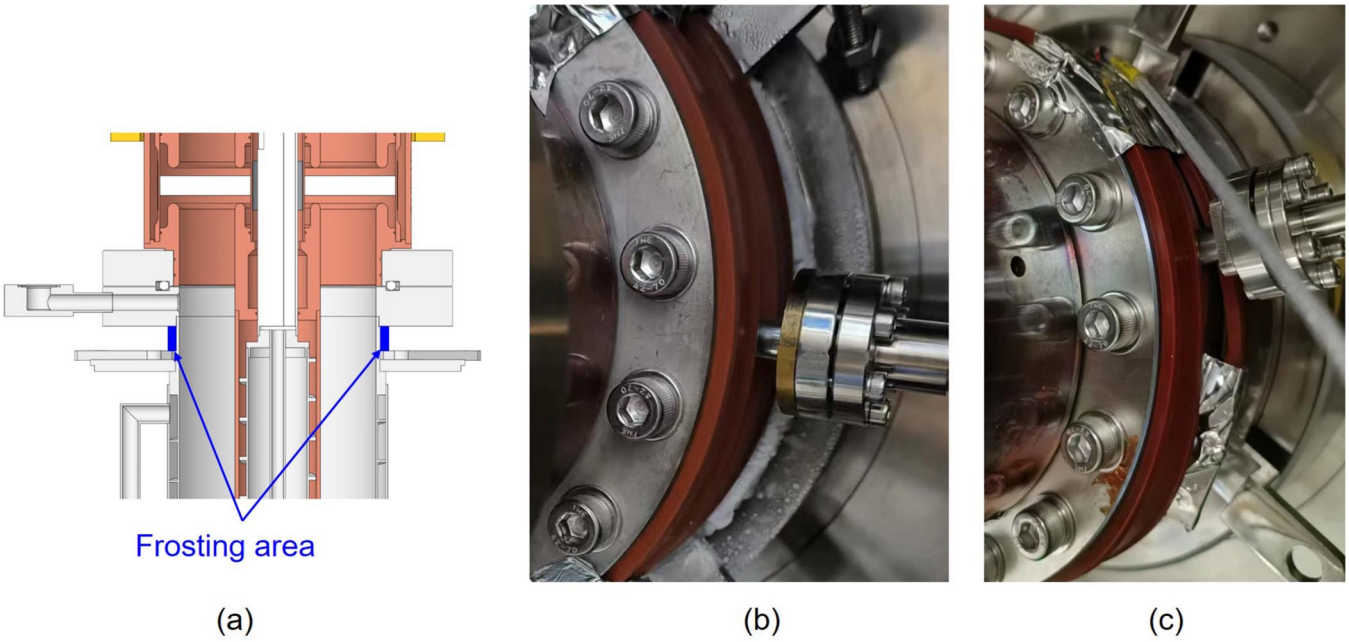


FIG. 22. Frosting issues in the FPCs: (a) frosting region highlighted in blue; (b) frosting observed in Series-A FPC; (c) elimination of frosting in the Series-B FPCs.

simulated and measured temperatures at the outer conductor near the cold flange (sensor "SO" noted in Fig. 20) together with the corresponding 4.2 K heat load contributed by the coupler. The measured temperature at sensor SO decreased markedly from 35 K at an accelerating voltage of 1.1 MV (PoP) to 14.2 K at 1.2 MV (CM1). Concurrently, the cryogenic heat load decreased from 11.1 to 3.0 W under the same operating conditions. In both tests, the helium-gas flow rate was maintained at 14 SLM, which was the highest achievable flow rate for the PoP tests. These reductions demonstrate the effectiveness of the design modifications in mitigating overheating in the cavity-coupler interface region. Both the measured temperature and heat load were higher than the simulated values, which is attributed to the combined effect of modeling uncertainties, nonideal thermal contact between flanges, and measurement errors.

The optimum helium-gas flow rate was further investigated by comparing the temperatures measured at the NbTi flange and the helium inlet pipe, together with the total cryogenic heat load of the module. As shown in Fig. 21, increasing the helium-gas flow rate above 30 SLM resulted in negligible changes in both the temperature rise and the total cryogenic heat load. However, when the flow rate was reduced to 20 SLM, the helium-gas inlet temperature increased from 4.3 to 7.2 K, while the temperature of the NbTi flange rose to 9.1 K, approaching the superconducting critical temperature of NbTi (8–10 K) [29,30].

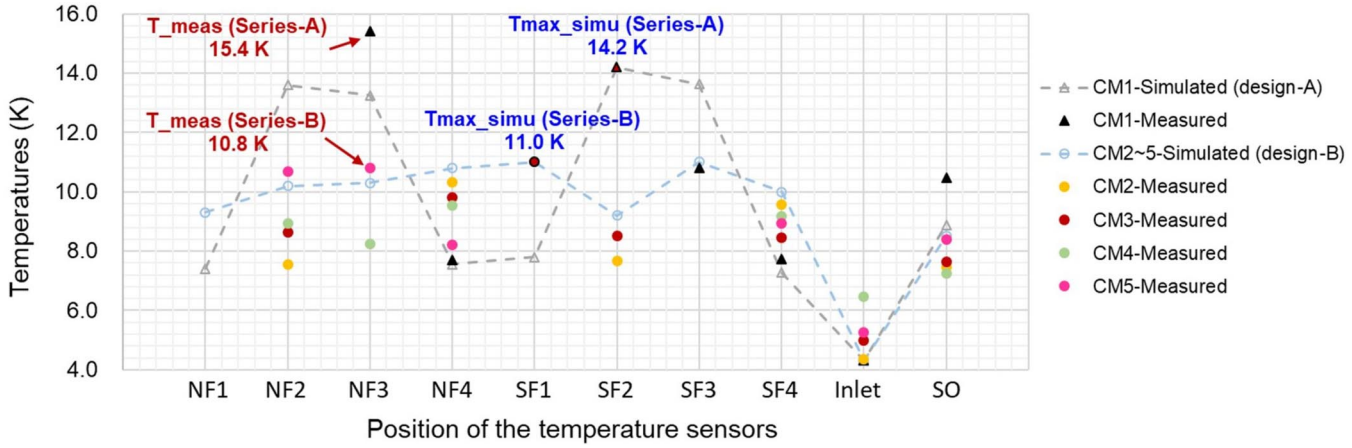


FIG. 23. Temperatures in the cavity-coupler interface region of five HOM-damped SRF modules operated at 1.2 MV with a helium-gas flow rate of 30 SLM for the FPC.

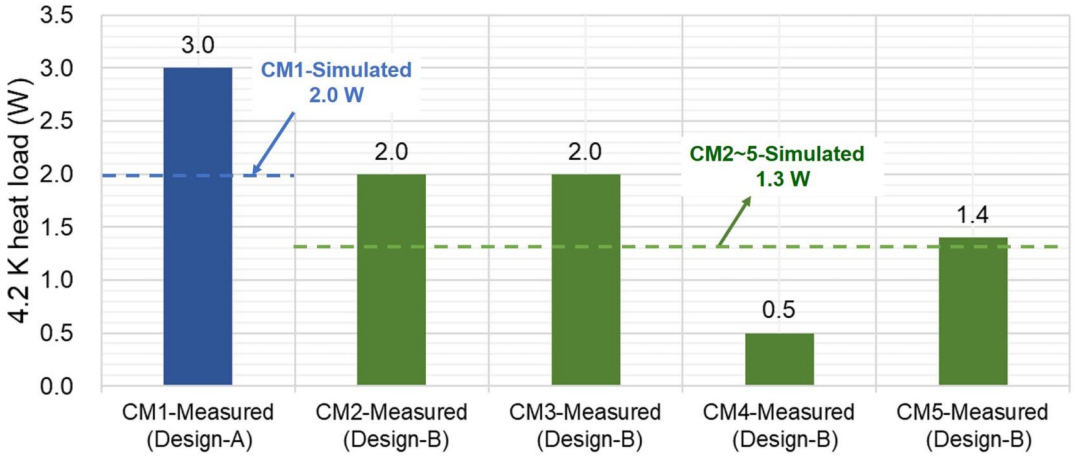


FIG. 24. Measured 4.2 K heat load contributed by the FPCs of five HOM-damped SRF modules operated at 1.2 MV with a helium-gas flow rate of 30 SLM.

Therefore, a helium-gas flow rate of 30 SLM was selected for subsequent tests and operation.

Since the outer conductor of the FPC is only 400 mm long, heating tapes were wrapped around the window-outer-conductor connecting flange to prevent ice and frost formation in this region. However, frosting was still observed near the rf window and the coupler-cryostat connecting flange [Fig. 22(a)] when the helium-gas flow rate was increased to 30 SLM, as shown in Fig. 22(b). Such frosting could potentially lead to vacuum leakage during long-term operation. Therefore, eliminating frost formation in this region became the key focus for further design improvement.

2. Series-B

For the Series-B FPCs, both the fin structure on the coupler-cryostat connecting flange and the helium-gas cooling outlet were relocated to mitigate the frosting observed during the CM1 horizontal test. These modifications proved effective. During the subsequent horizontal tests of the four SRF modules (CM2–CM5), frosting around the rf window was eliminated, as shown in Fig. 22(c).

In addition, a further reduction in the temperature rise of the cavity-coupler interface region was expected in the Series-B FPCs by rotating the helium-gas cooling inlet by 90° clockwise relative to the Series-A configuration. Figure 23 presents the simulated and measured temperatures

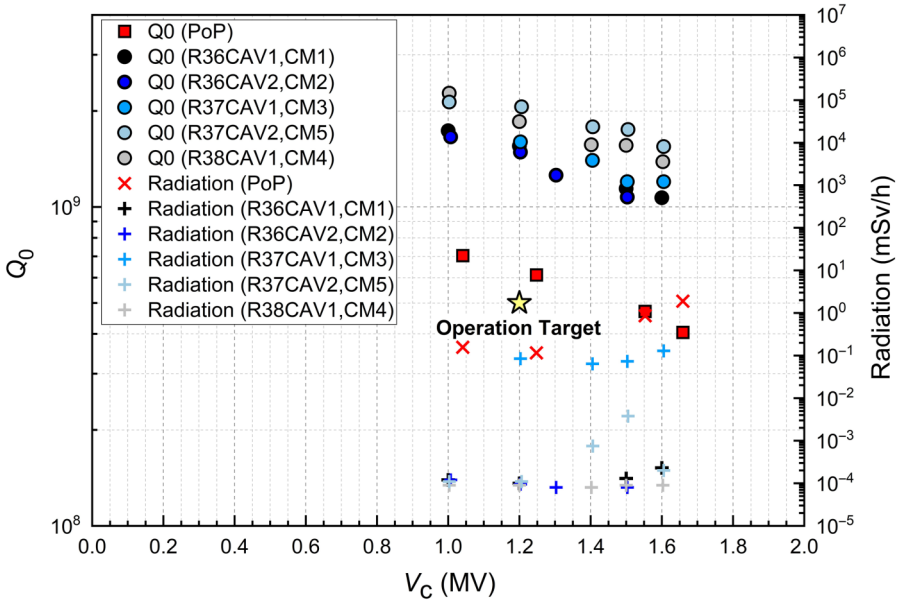


FIG. 25. Quality factors (Q_0) and radiation levels of the 166.6 MHz PoP cavity measured in a test cryostat and the 166.6 MHz HOM-damped cavity modules measured at the horizontal test stand.

in the cavity-coupler interface region of the five 166.6 MHz SRF modules operated at 1.2 MV with a helium-gas flow rate of 30 SLM. From Series-A to Series-B, the simulated maximum temperature decreased from 14.2 to 11.0 K, while the temperature measured at "NF3" decreased from 15.4 to 10.8 K. The NF3 location was selected for comparison because its temperature is least sensitive to the helium inlet position among all monitored points on the NbTi flange. Figure 24 presents the measured 4.2 K heat loads contributed by the FPCs in CM1 (Series-A) and CM2–CM5 (Series-B). The heat load decreased from 3.0 W in CM1 to 0.5–2.0 W in the Series-B modules, with an average value of 1.5 W, corresponding to approximately 4% of the module's total heat load. These results confirm the effectiveness of the Series-B modifications. Nevertheless, discrepancies remained between the measured and simulated values, likely due to a combination of modeling uncertainties and measurement errors.

A more direct demonstration of these continuous improvements is the substantially enhanced performance of the entire SRF modules [27]. Figure 25 presents the unloaded quality factor Q_0 and radiation levels of all 166.6 MHz SRF modules measured at the horizontal test stand over a range of accelerating voltages. The results show that the Q_0 values of the five production modules equipped with Series FPCs exceeded 1×10^9 at 1.5 MV, more than twice that of the PoP module (4×10^8 at 1.5 MV). In addition, the radiation level decreased from several thousand μSv/h in the PoP module to below 10 μSv/h in the production modules, except for CM3, where it remained at several tens of. This relatively higher radiation level was likely associated with contamination introduced during multiple assembly attempts required to resolve defective knife-edge flange issues. The reduction in radiation level can be attributed, at least in part, to the improved cleanliness enabled by performing the entire on-stand testing process of the series FPCs under cleanroom conditions.

V. HIGH-POWER OPERATION WITH BEAM

The successful on-cavity tests of the series FPCs qualified them for beam operation in the HEPS storage ring. This section presents their performance during subsequent beam commissioning and routine operation.

Beam commissioning of HEPS, employing five 166.6 MHz SRF modules to accelerate a 6 GeV electron beam, started in August 2025. The beam current was gradually increased, reaching 100 mA (key performance parameter) on September 12, 2025, and 150 mA on March 7, 2026. During beam commissioning, all five 166.6 MHz FPCs showed excellent rf, vacuum, and thermal performance. Figure 26 presents the main operating parameters of the five FPCs at a beam current of 150 mA during the latest commissioning period. A total forward rf power of 508 kW was delivered through the five 166.6 MHz FPCs, with each FPC transmitting a maximum forward power of up to 116 kW. All 166.6 MHz couplers consistently maintained vacuum pressures below 2.5×10^{-7} Pa. The ceramic-window temperature remained below 29.0°C, while the maximum temperature of the air section inside the inner T-box was maintained at 41.0°C under a tunnel ambient temperature of 26.0°C. Meanwhile, the average

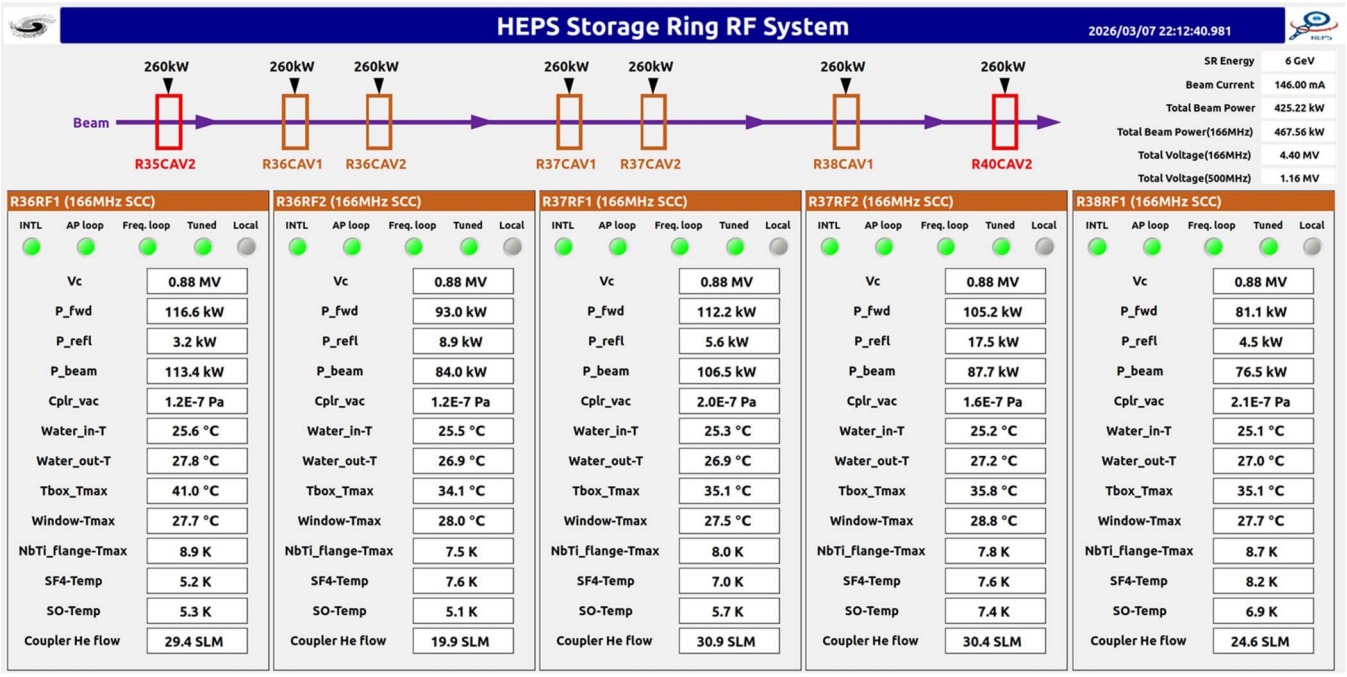


FIG. 26. Critical parameters of the FPCs operating at a beam current of 150 mA.

cooling water temperature rise was measured to be 1.8°C, corresponding to an estimated rf power dissipation of 420 W in the coupler's inner conductor.

The maximum temperature measured at the NbTi flange near the FPC port was maintained below 9.0 K, and the average temperature measured at the coupler's outer conductor near the cold flange (sensor SO in Fig. 20) was approximately 6.1 K. These temperature measurements confirm the adequacy of the coupler cooling design and demonstrate the effectiveness of the design improvements in mitigating overheating in the cavity-coupler interface region. In addition, it is noteworthy that multipacting activity was rarely observed, and the arc discharges typically associated with such events were seldom triggered throughout the beam commissioning and operation period.

VI. CONCLUSIONS

A series of 166.6 MHz fundamental power couplers for the HEPS quarter-wave $\beta = 1$ superconducting rf cavities has been developed, evolving from prototype to series production. Prototype testing identified overheating in the cavity-coupler interface region as the primary cause of severe quality-factor degradation and cavity quenching. The Series-A design mitigated this issue through an extended niobium coupler port and optimized helium-gas cooling. In addition, the maximum temperature of the coupler, located at the inner T-box, was significantly reduced by implementing a jet-impingement air-cooling scheme. Subsequent testing of the CM1 validated these improvements but revealed a frosting issue near the rf window. This issue was subsequently eliminated in Series-B through relocation of the fin structure and helium outlet. Furthermore, by rotating the helium inlet by 90°, the measured maximum temperature in the cavity-coupler interface region decreased from 15.4 to 10.8 K, while the average heat load at 4.2 K was reduced by half, to 1.5 W.

All 10 series FPCs were successfully validated through on-stand tests up to 250 kW cw in traveling-wave mode and on-cavity tests up to 120 kW cw in standing-wave mode. Five FPCs are currently operating stably in the HEPS storage ring at a beam current of 150 mA, with a single FPC transmitting up to 116 kW, representing the highest demonstrated beam-operation power level to date for FPCs used in TEM-type SRF cavities. The development of the HEPS 166.6 MHz FPCs demonstrates that the challenges associated with on-cell couplers for TEM-type SRF cavities, although more demanding than those for beam-pipe-mounted couplers used in elliptical SRF cavities, can be effectively overcome through systematic design optimization and iterative improvement. This work expands the demonstrated capability of nonelliptical SRF cavities for high-current accelerator applications. The design approaches and operational experience gained from this work provide valuable references for other superconducting structures requiring on-cavity high-power feeding.

ACKNOWLEDGMENTS

We would like to thank colleagues from the HEPS Cryogenics System for designing the cryostat and their technical support in cavity vertical tests, cryomodule assembly, and horizontal tests at PAPS, as well as for their support in tunnel installation, commissioning, and operation at HEPS. We also acknowledge the support from the Utility Division regarding transportation, installation, and conventional cooling for the modules. Funding was received from the National Natural Science Foundation of China (Grants No. 12275285, No. 12475166, No. 12275287, and No. 12575159). This work was supported by the High Energy Photon Source, a major national science and technology infrastructure in China, funded by the National Development and Reform Commission (NDRC) of China.

DATA AVAILABILITY

There are no publicly available research data or software supporting this manuscript. Requests for further information or data should be sent to the authors.

[1] Y. Jiao, G. Xu, X. H. Cui, Z. Duan, Y. Y. Guo, P. He, D. H. Ji, J. Y. Li, X. Y. Li, C. Meng, Y. M. Peng, S. K. Tian, J. Q. Wang, N. Wang, Y. Y. Wei, H. S. Xu, F. Yan, C. H. Yu, Y. L. Zhao, and Q. Qin, The HEPS project, J. Synchrotron Radiat. **25**, 1611 (2018).

[2] H. Xu *et al.*, Equilibrium electron beam parameters of the High Energy Photon Source, Radiat. Detect. Technol. Methods **7**, 279 (2023).

[3] H. Xu *et al.*, First beam storage in the High Energy Photon Source storage ring, Radiat. Detect. Technol. Methods **9**, 70 (2025).

[4] P. Zhang, J. Dai, Z. Deng, L. Guo, T. Huang, D. Li, J. Li, Z. Li, H. Lin, Y. Luo, Q. Ma, F. Meng, Z. Mi, Q. Wang, H. Xu, X. Zhang, F. Zhao, and H. Zheng, Radio-frequency system of the high energy photon source, Radiat. Detect. Technol. Methods **7**, 159 (2023).

[5] S. Mitsunobu, T. Furuya, T. Tajima, T. Kijima, and T. Tanaka, High power input coupler for KEKB superconducting cavities, in *Proc. 9th Workshop on RF Superconductivity (SRF'99)* (JACoW, Santa Fe, NM, USA, 1999), pp. 505–507.

[6] E. Montesinos, Construction and processing of the variable RF power couplers for the LHC superconducting cavities, in *Proc. 13th Int. Conf. RF Superconductivity (SRF'07)* (JACoW, Beijing, China, 2007), pp. 646–650.

[7] W. Xu, Z. A. Conway, J. M. Fite, D. Holmes, K. S. Smith, and A. Zaltsman, High power coupler development for EIC, in *Proc. 20th Int. Conf. RF Superconductivity (SRF'21)* (JACoW Publishing, Geneva, Switzerland, East Lansing, MI, USA, 2022), pp. 632–636.

[8] D. Regidor *et al.*, LIPAc SRF linac couplers conditioning, in *Proc. 5th International Particle Accelerator Conference (IPAC'14), International Particle Accelerator Conference No. 5* (JACoW, Geneva, Switzerland, 2014), pp. 2562–2564,10.18429/JACoW-IPAC2014-WEPRI039.

[9] N. Bazin, S. Chel, G. Devanz, T. Ebisawa, H. Jenhani, G. Phillips, O. Piquet, D. Regidor, and F. Toral, Status of the IFMIF/EVEDA Superconducting Linac, in *Proc. SRF'19, International Conference on RF Superconductivity No. 19* (JACoW Publishing, Geneva, Switzerland, 2019), pp. 735–741, 10.18429/JACoW-SRF2019-WETEA3.

[10] T. Jiang, F. Bai, Y. He, Z. Lin, Y. Wan, R. Wang, Z. Wang, M. Xu, and S. Zhang, The development of a prototype fundamental power coupler for CiADS and HIAF half wave resonators, in *Proc. SRF'21, International Conference on RF Superconductivity No. 20* (JACoW Publishing, Geneva, Switzerland, 2022), pp. 295–298.

[11] T. Cabanel, Y. G. Martinez, D. Marchand, R. Micoud, F. Pancher, D. Tourres, and F. Vezzu, SPIRAL 2 coupler preparation and RF conditioning, in *Proc. 13th Int. Conf. RF Superconductivity (SRF'07)* (JACoW Publishing, Geneva, Switzerland, 2007), pp. 446–449.

[12] T. Junquera, G. Olry, H. Saugnac, J. Biarrotte, S. Blivet, S. Bousson, C. Commeaux, M. Fruneau, Y. Gomez, E. Vernay, F. Vezzu, and P. Balleyguiere, High intensity linac driver for the SPIRAL-2 project: Design of superconducting 88 MHz quarter wave resonators (beta 0.12), power couplers and cryomodules, in *Proc. 9th European Particle Accelerator Conf. (EPAC'04)* (JACoW Publishing, Geneva, Switzerland, 2004), pp. 1285–1287.

[13] N. Solyak, B. Hanna, J. Helsper, S. Kazakov, D. Passarelli, and S. Wallon, Testing and processing of pre-production 325 MHz single spoke resonator power couplers for PIP-II project, in *Proc. 21th Int. Conf. RF Supercond. (SRF'23), International Conference on RF Superconductivity No. 21* (JACoW Publishing, Geneva, Switzerland, 2023), pp. 816–819.

[14] Z. Zheng, J. Popielarski, K. Saito, S. Stark, T. Xu, and Y. Yamazaki, Design and commissioning of FRIB multipacting-free fundamental power coupler, in *Proc. of Linear Accelerator Conference (LINAC'16), East Lansing, MI, USA, 25-30 September 2016 Linear Accelerator Conference No. 28* (JACoW, Geneva, Switzerland, 2017), pp. 767–769, 10.18429/JACoW-LINAC2016-THOP10.

[15] H. Li, M. Jobs, R. Santiago Kern, V. Goryashko, L. Hermansson, A. Bhattacharyya, T. Lofnes, K. Gajewski, K. Fransson, and R. Ruber, Characterization of a $\beta = 0.5$ double spoke cavity with a fixed power coupler, Nucl. Instrum. Methods Phys. Res., Sect. A **927**, 63 (2019).

[16] M. Fan *et al.*, Development of the fundamental power coupler for 324 MHz superconducting cavities, Phys. Rev. Accel. Beams **26**, 090401 (2023).

[17] T. Huang, P. Zhang, Q. Ma, H. Lin, Q. Wang, W. Pan, F. Bing, K. Gu, and L. Guo, Development of fundamental power couplers for 166.6 MHz superconducting quarter-wave beta = 1 proof-of-principle cavities, Rev. Sci. Instrum. **91**, 063301 (2020).

[18] W. Xu *et al.*, Design, simulations, and conditioning of 500 kw fundamental power couplers for a superconducting rf gun, Phys. Rev. ST Accel. Beams **15**, 072001 (2012).

[19] T. Huang, P. Zhang, Z. Chang, Q. Ma, X. Zhang, Z. Li, R. Han, Q. Wang, H. Lin, J. Zhou, R. Ge, and W. Pan, High-power tests and solution to overheating at cavity–coupler interface of the 166.6-MHz beta = 1 superconducting quarter-wave resonator for HEPS, AIP Adv. **11**, 045024 (2021).

[20] X. Zhang, P. Zhang, Z. Li, Q. Wang, H. Lin, Z. Mi, Q. Ma, W. Pan, J. Dai, T. Huang, R. Han, R. Ge, L. Sun, F. Meng, and D. Li, Design and mechanical performance of a dressed 166.6 MHz $\beta = 1$ proof-of-principle superconducting cavity in horizontal tests, IEEE Trans. Appl. Supercond. **30**, 1 (2020).

[21] CST Studio Suite®, Release 2021, https://www.3ds.com/products/simulia/cst-studio-suite.

[22] ANSYS®, Release 17.2, ANSYS Inc.., http://www.ansys.com.

[23] P. Zhang, X. Zhang, Z. Li, J. Dai, L. Guo, H. Lin, Q. Ma, T. Huang, Z. Mi, Q. Wang, and F. Meng, Development and vertical tests of a 166.6 MHz proof-of-principle superconducting quarter-wave beta = 1 cavity, Rev. Sci. Instrum. **90**, 084705 (2019).

[24] X. Zhang, P. Zhang, Z. Li, J. Dai, X. Hao, Q. Ma, T. Huang, H. Lin, Z. Mi, Q. Wang, and F. Meng, The mechanical design, fabrication and tests of a 166.6 MHz quarter-wave beta = 1 proof-of-principle superconducting cavity for HEPS, Nucl. Instrum. Methods Phys. Res., Sect. A **947**, 162770 (2019).

[25] L. Guo, P. Zhang, X. Zhang, J. Dai, Z. Mi, Q. Ma, and F. Meng, Development of a 166.6 MHz $\beta = 1$ higher-order-mode-damped superconducting cavity, Rev. Sci. Instrum. **95**, 074702 (2024).

[26] X. Zhang, P. Zhang, Q. Ma, L. Guo, H. Zheng, F. Meng, Z. Mi, T. Huang, and J. Dai, Compact design of the 166.6 MHz superconducting cavity and its beamline elements for HEPS, Nucl. Instrum. Methods Phys. Res., Sect. A **1059**, 168972 (2024).

[27] P. Zhang, X. Zhang, L. Guo, Q. Ma, J. Dai, T. Huang, H. Zheng, F. Meng, Z. Mi, H. Lin, Q. Wang, D. Li, F. Zhao, S. Jin, and J. Li, Development and high-current cw operation of 166.6 MHz high-power, higher-order-modes-damped $\beta = 1$ quarter-wave srf modules at the high energy photon source, Phys. Rev. Accel. Beams **29**, 032002 (2026).

[28] Z. Deng, P. Zhang, T. Huang, Q. Wang, H. Lin, J. Dai, Q. Ma, L. Xiao, and W. Pan, Development of an automatic control and analysis system for the conditioning of high-power couplers at IHEP, J. Instrum. **16**, P07027

[29] M. Ikebe, S. Nakagawa, K. Hiraga, and Y. Muto, Anomalous phonon thermal resistivity in superconducting $Ti_{55}Nb_{45}$ alloys, Solid State Commun. **23**, 189 (1977).

[30] H. Takei, Electrical resistivity of Nb-Ti superconductors, Trans. Jpn. Inst. Met. **25**, 511 (1984).